Journal of Controlled Release 356 (2023) 416–433

Contents lists available at ScienceDirect

Journal of Controlled Release

journal homepage: www.elsevier.com/locate/jconrel

Hydrogel-forming microarray patches with solid dispersion reservoirs for transdermal long-acting microdepot delivery of a hydrophobic drug

Yara A. Naser [a], Ismaiel A. Tekko [a,b], Lalitkumar K. Vora [a], Ke Peng [a], Qonita K. Anjani [a], Brett Greer [c], Christopher Elliott [c], Helen O. McCarthy [a], Ryan F. Donnelly [a,*]

[a] School of Pharmacy, Queen's University Belfast, Medical Biology Centre, 97 Lisburn Road, Belfast BT9 7BL, UK
[b] Department of Pharmaceutics and Pharmaceutical Technology, Faculty of Pharmacy, Aleppo University, Aleppo, Syria
[c] Institute for Global Food Security, School of Biological Science, Queen's University Belfast, 19 Chlorine Gardens, Belfast BT9 5DL, UK

ARTICLE INFO

Keywords:
Solid dispersion
Hydrogel-forming microarray patch
Microneedles
Transdermal drug delivery
Long-acting depot
PEG
Atorvastatin

ABSTRACT

Hydrogel-forming microarray patches (HF-MAPs) are used to circumvent the skin barrier and facilitate the noninvasive transdermal delivery of many hydrophilic substances. However, their use in the delivery of hydrophobic agents is a challenging task. This work demonstrates, for the first time, the successful transdermal long-acting delivery of the hydrophobic atorvastatin (ATR) *via* HF-MAPs using poly(ethylene)glycol (PEG)-based solid dispersion (SD) reservoirs. PEG-based SDs of ATR were able to completely dissolve within 90 s *in vitro*. *Ex vivo* results showed that 2.05 ± 0.23 mg of ATR/0.5 cm^2 patch was delivered to the receiver compartment of Franz cells after 24 h. The *in vivo* study, conducted using *Sprague Dawley* rats, proved the versatility of HF-MAPs in delivering and maintaining therapeutically-relevant concentrations (> 20 $ng{\cdot}mL^{-1}$) of ATR over 14 days, following a single HF-MAP application for 24 h. The long-acting delivery of ATR suggests the successful formation of hydrophobic microdepots within the skin, allowing for the subsequent sustained delivery as they gradually dissolve over time, as shown in this work. When compared to the oral group, the use of the HF-MAP formulation improved the overall pharmacokinetics profile of ATR in plasma, where significantly higher AUC values resulting in ~10-fold higher systemic exposure levels were obtained. This novel system offers a promising, minimally-invasive, long-acting alternative delivery system for ATR that is capable of enhancing patient compliance and therapeutic outcomes. It also proposes a unique promising platform for the long-acting transdermal delivery of other hydrophobic agents.

1. Introduction

The popularity of long-acting drug delivery systems has significantly increased over the last few decades, due to the advantages they offer over conventional systems [1]. Sustained release dosage forms are designed to achieve an extended therapeutic effect by continuously releasing medications over a prolonged period following a single dose administration [2]. Long-acting dosage forms can possess many advantages, including reducing undesired fluctuations of drug levels in plasma, reducing the dosing frequency and, therefore, improving patients' compliance [2–4]. However, to achieve sustained release for over 24 h, injections or implants are generally needed. In addition to being painful and invasive, injections possess many other drawbacks. These include the sterility requirements for a parenteral product, which can increase the costs and challenges in developing and manufacturing a sustained-release product for parenteral delivery [5]. On the other hand, implants are invasive and, if not biodegradable, require surgical removal. Furthermore, they might increase the risk of polymer accumulation in the body after use [6]. Therefore, it is essential to utilize another route that could be more appealing to patients to ensure their compliance with their dose regimens. This alternative route should possess the ability to deliver drugs that cannot be easily administered orally. An ideal drug delivery method would possess the simplicity of oral administration (self-administered), along with the high bioavailability associated with the parenteral route [7]. Transdermal drug delivery (TDD) is a candidate approach employed to deliver various drugs

Abbreviations: PEG, Poly(ethylene) glycol; SD, Solid dispersion; HF-MAPs, Hydrogel-forming microarray patches; ATR, Atorvastatin; TDD, Transdermal drug delivery.

* Corresponding author at: School of Pharmacy - Queen's University Belfast, Medical Biology Centre, 97 Lisburn Road, Belfast BT9 7BL, UK.
E-mail address: r.donnelly@qub.ac.uk (R.F. Donnelly).

https://doi.org/10.1016/j.jconrel.2023.03.003
Received 19 July 2022; Received in revised form 24 February 2023; Accepted 2 March 2023
Available online 13 March 2023

through the skin for therapeutic use as a promising alternative to oral and parenteral routes of administration [8].

TDD offers several advantages over conventional administration methods, being a painless mode of drug delivery that can bypass first-pass metabolism and provide improved patient accessibility and compliance compared to oral and parenteral drug routes [9,10]. It can avoid first-pass metabolism, resulting in reduced side effects following transdermal administration compared to similar oral doses [11,12]. However, due to the fierce barrier characteristics of the *stratum corneum* (SC); the outermost layer of the skin, and the major barrier against TDD, the number of drugs that can be delivered across the skin is very limited [13,14]. Therefore, only fairly lipophilic drug substances (LogP 1–3), possessing low molecular weights (< 500 Da), high potencies, and displaying relatively low melting points can be delivered [15]. Consequently, fewer than 20 active pharmaceutical agents are commercially delivered through the skin, mainly in the form of transdermal patches [16]. One way to overcome this obstacle in the field of TDD is the use of microarray patches (MAPs).

Hydrogel-forming MAPs (HF-MAPs) are micron-sized minimally invasive devices capable of penetrating the *SC* without causing any pain or bleeding [17–19]. This grants them the ability to facilitate the delivery of multiple therapeutic agents across the skin [20]. HF-MAPs are made from crosslinked polymers and are typically devoid of any drug [11,12,14,21,22]. Therefore, a separate drug reservoir must be attached to their upper surfaces. Once inserted into the skin, HF-MAPs can imbibe the interstitial fluid and, thus, swell to form temporary unblockable conduits between the microcirculation and the drug-containing reservoir placed on the top of the patch (Fig. 1) [12]. HF-MAPs are capable of imbibing large quantities of water and swelling due to the presence of hydrophilic functional groups on their polymeric backbone [23]. Despite their high content of water, reaching up to 99% of their total weight once swollen, HF-MAPs are capable of maintaining their physical and chemical structure integrity due to the crosslinking of individual polymer chains; thus, they are not prone to dissolve in water [24–26]. As they pierce the *SC*, HF-MAPs function as a rate-controlling membrane, allowing for a controlled release of the drug from the reservoir into the body [12]. The rate of drug release and delivery from the reservoirs relies mainly on the degree of crosslinking between the polymers, which can also control the swelling rate of the hydrogels themselves [11,27]. This unique design of HF-MAPs possesses inherent benefits, as it overcomes the limitations of dissolving polymeric MAPs [28]. For instance, the drug loading of many therapeutic agents is not limited to the capacity of the MAPs themselves. However, it now relies on the crosslinking density of the hydrogel system [11]. Moreover, HF-MAPs can be fabricated into a wide range of patch sizes and microarray geometries, and they are easy to sterilize [13,14]. Additionally, they can be removed from the skin completely intact following their insertion, with no polymer residues left behind [11]. A further advantage is that upon their removal, HF-MAPs are swollen and soft, so the risk of mistaken reinsertion is minimal [22]. Due to all these aforementioned advantages, this promising technology was shown to possess the ability to broaden the range of types of drugs delivered transdermally, without mislaying the benefits of this route for industry, healthcare providers, and patients themselves [11].

HF-MAPs could successfully deliver a wide variety of hydrophilic molecules, including ibuprofen sodium, insulin, proteins, antibodies, metformin hydrochloride, metronidazole, esketamine and, most recently, amoxicillin [11,12,29–32]. However, neither the administration of hydrophobic agents nor long-acting drug delivery utilizing HF-MAPs for periods longer than 48 h has previously been documented. Indeed, approximately 40% of the marketed drugs and 90% of the compounds in the drug discovery pipeline are lipophilic molecules and require relatively high doses [33–36]. Delivering such drugs is promising, as their lipophilicity can be used in sustaining their release to obtain a long-acting effect. However, their delivery using HF-MAPs is difficult due to the hydrophilic nature of the hydrogels themselves. Therefore, in order to successfully deliver a hydrophobic agent, its solubility will need to be enhanced first.

Solid dispersion (SD) is a widely used solubility enhancement technique. It was first introduced by Sekiguchi and Obi early in the 1960s [37,38]. The SD method is defined as the dispersion of a hydrophobic molecule in one or more hydrophilic matrices, and thus improves the molecule's solubility by increasing its surface area and wettability [39]. Some of the most frequently used hydrophilic carriers include poly (vinyl)pyrrolidone (PVP) [40,41], poly(ethylene) glycols (PEG) [42–44], and polymethacrylates [45,46]. PEG has been extensively utilized in preparing SDs of hydrophobic drugs due to its high biocompatibility, low melting points, especially for solid PEGs with lower molecular weights, and its well-established safety profile [47–49].

In this study, atorvastatin (ATR) was chosen as the model hydrophobic agent to investigate the long-acting delivery potential using HF-MAPs. ATR is an orally administered drug that is available as tablets and given in dosages of 10–80 mg·day^{-1} to prevent and treat hyperlipidemia. It is considered to be the most prescribed statin in the world [50].

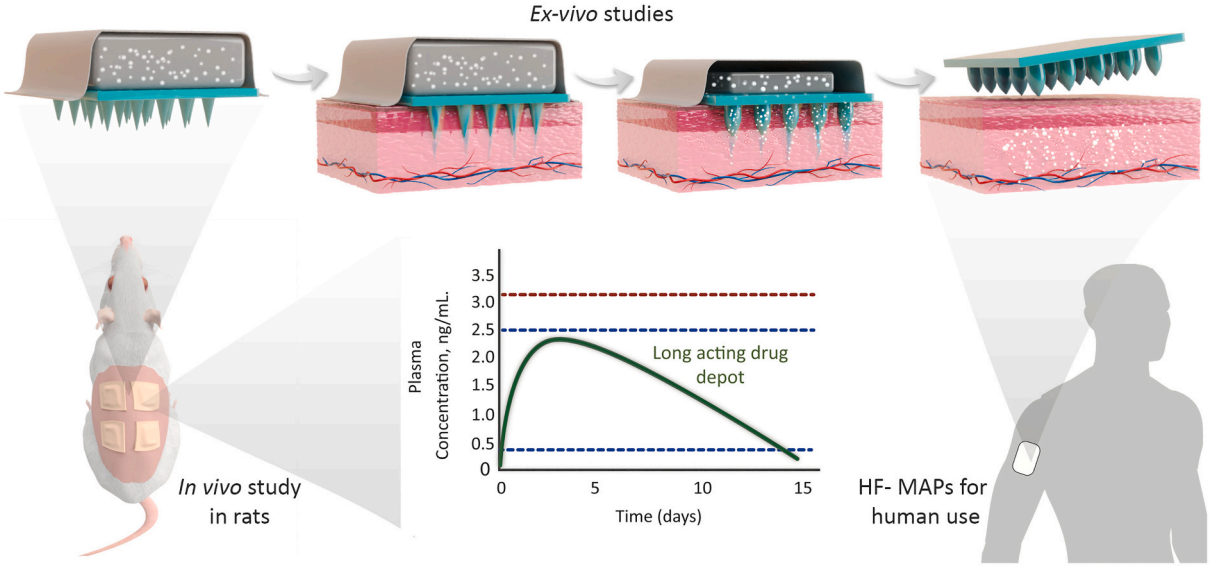

Fig. 1. A schematic depiction of HF-MAPs with PEG-based SD reservoirs used for the long-acting delivery of the hydrophobic antihyperlipidemic ATR.

ATR undergoes extensive first-pass metabolism in the liver, which results in its low oral bioavailability of 12–14% [51]. Furthermore, ATR falls in class II Biopharmaceutical Classification System (BCS) drug category, meaning that it has poor water solubility and high permeability [51,52]. As a poorly water-soluble compound, the dispersion of ATR into the PEG matrix would represent an appealing approach to increase its permeation across the skin *via* HF-MAP. Moreover, the SD technique could be beneficial in enhancing the dissolution rate and, thus, the permeability of this class II BCS compound.

Herein, this work presents for the first time, the successful utilization of PEG-based SD reservoirs assembled with HF-MAPs for the efficient long-acting transdermal deposition and delivery of the hydrophobic ATR. The *in vivo* study, conducted using *Sprague Dawley* rats as an animal model, showed the versatility of this system to achieve long-acting delivery of hydrophobic ATR, for 2 weeks following a single dose application for 24 h. Due to the hydrophobic nature of ATR, it would not have been abruptly taken up by the dermal microcirculation into the blood stream. Most of it would have remained under the skin and created a microdepot, from which the long-acting effect was observed following a single dose application. This novel system has the potential to offer a promising minimally invasive long-acting alternative delivery method for hydrophobic agents. Therefore, it can enhance patients' compliance with their treatment regimens and, thus, improve the therapeutic outcomes of drugs and enhance the patients' quality of life (Fig. 1).

2. Materials and methods

2.1. Materials

Atorvastatin hemicalcium trihydrate was purchased from Cangzhou Enke Pharma-tech Co., Limited, Hebei Province, China. Gantrez® S-97, a copolymer of methylvinylether and maleic acid (PMVE/MA) with a molecular weight of 1500 kDa, was gifted by Ashland, Kidderminster, UK. Poly (ethylene glycol) (PEG) with average MWs of 10,000, 8000, 6000, 600, 400, and 200 Da, methanol and acetonitrile for high-performance liquid chromatography (HPLC), phosphate-buffered saline (PBS) pH 7.4 tablets, and sodium carbonate (Na_2CO_3) were all purchased from Sigma–Aldrich, Dorset, UK. All other chemicals used were of analytical reagent grade.

2.2. Fabrication and characterization of hydrogel-forming MAPs

Four hydrogel formulations were considered, as shown in Table 1. The main element of all those formulations was Gantrez® S-97, a copolymer of methylvinylether and maleic acid (PMVE/MA). A stock of 40% *w*/w Gantrez® S-97 was initially prepared by the slow addition of the required mass of Gantrez® S-97 powder to deionized water. The mixture was stirred to homogeneity. It was then stored in a 4 °C refrigerator and used within a month. This stock was used to obtain the concentration of Gantrez® S-97 required to fabricate the hydrogel films and MAPs.

The formulations were prepared by dissolving the required percentages of PEG 10,000 in small volumes of deionized water before mixing with the appropriate mass of Gantrez® S-97, as shown in Table 1. Na_2CO_3 was initially ground using a mortar and pestle until a fine powder was obtained prior to its addition as the last step in F4 preparation. Deionized water was added to reach up to 100% (*w*/w) of the required mass. The aqueous blends were then centrifuged at 5000 rpm for 5 min to remove any trapped air bubbles and ensure the homogeneity of the hydrogels. The centrifuged hydrogel blends were cast in laser engineered silicone micromoulds, as previously reported [17]. The moulds consisted of 361 (19 × 19) microneedles (MNs) perpendicular to the baseplate and of conical shape with a height of 600 μm, baseplate width of 300 μm and MNs interspacing of 50 μm on a 0.5 cm^2 area. In each mould, a mass of 500 mg of the aqueous blend of the corresponding hydrogel formulation was carefully dispensed. The moulds were subsequently centrifuged at 3500 rpm for 20 min to ensure that the gels were homogeneously distributed into the microcavities of the moulds and to remove any surface bubbles that might affect the formulation. They were then left to dry for 48 h at room temperature prior to crosslinking in an 80 °C oven for 24 h. The HF-MAPs were then removed from the oven and demolded, then their sidewalls were removed using a hot blade. Fig. 2(A-D) summarizes the preparation process of HF-MAPs.

Table 1
The four different aqueous blends used in the preparation of the hydrogel films initially explored.

Formulation	Gantrez® S-97 *(w/w)*	PEG 10,000 *(w/w)*	Na_2CO_3 *(w/w)*
F1	20%	10%	0%
F2	20%	7.5%	0%
F3	15%	7.5%	0%
F4	20%	7.5%	3%

2.2.1. Mechanical characterization of HF-MAPs

The mechanical properties of the HF-MAPs were examined using a TA.XT2 Texture Analyzer in compression mode, as reported previously [12,17]. HF-MAPs were visualized using a Leica EZ4D light microscope (Leica, Wetzlar, Germany) before testing, and the heights of at least five MNs from each side of the patch were manually determined. HF-MAPs were carefully attached to a moveable cylindrical probe (length 5 cm, cross-sectional area 1.5 cm^2), descending from the upper arm of the device using double-sided adhesive tape, with the needles pointing downwards. The test was conducted by pressing HF-MAPs against a flat stainless-steel baseplate at a 32 N force per patch and a pace of 0.5 mm/s for 30 s. Subsequently, HF-MAPs were gently removed from the probe and examined using the light microscope to measure their heights and determine the height reduction percentage using Eq. 1, where H_0 and H_1 resemble their heights before and after applying a 32 N force for 30 s, respectively.

$$Height\ reduction\% = \frac{H0 - H1}{H0} \cdot 100\% \quad (1)$$

2.2.2. Evaluation of HF-MAP insertion properties in vitro and ex vivo

The insertion efficiency of HF-MAPs was evaluated using Parafilm® M as a previously validated skin surrogate for insertion studies [53]. A sheet of Parafilm® M was cut into eight identical pieces stacked on top of each other to form an eight-layer film with an approximate thickness of 1 mm. The film was then placed on the stainless-steel baseplate, and HF-MAPs were attached with caution to the flat surface of the probe descending from the upper arm of the Texture Analyzer in compression mode. The probe was lowered onto the Parafilm® M layers at a pretest speed of 1.19 $mm.sec^{-1}$ until it achieved a preset force of 32 N. The force was held for 30 s at 32 N. Subsequently, the implanted HF-MAPs were removed, the Parafilm® M sheets were separated, and the number of holes generated in each layer was manually counted using a light microscope. The insertion percentage was calculated using Eq. 2 below.

$$Insertion\% = \frac{number\ of\ holes\ observed}{number\ of\ arrays\ in\ a\ MAP\ (361\ array)}\ x\ 100\% \quad (2)$$

The height reduction percentage of the HF-MAPs following the Parafilm® M insertion test was also determined using Eq. 1, where the heights of 5 MNs from each side were recorded prior to and post the insertion test.

An optical coherence tomography (OCT) microscope (EX1301 VivoSight®, Michelson Diagnostics Ltd., Kent, UK) was used to assess the insertion of HF-MAPs into full-thickness excised neonatal porcine skin *ex vivo*. It was used as a simulant of human skin due to the similarities between their properties [53]. The heights of the implanted MNs were measured using ImageJ® software (National Institutes of Health,

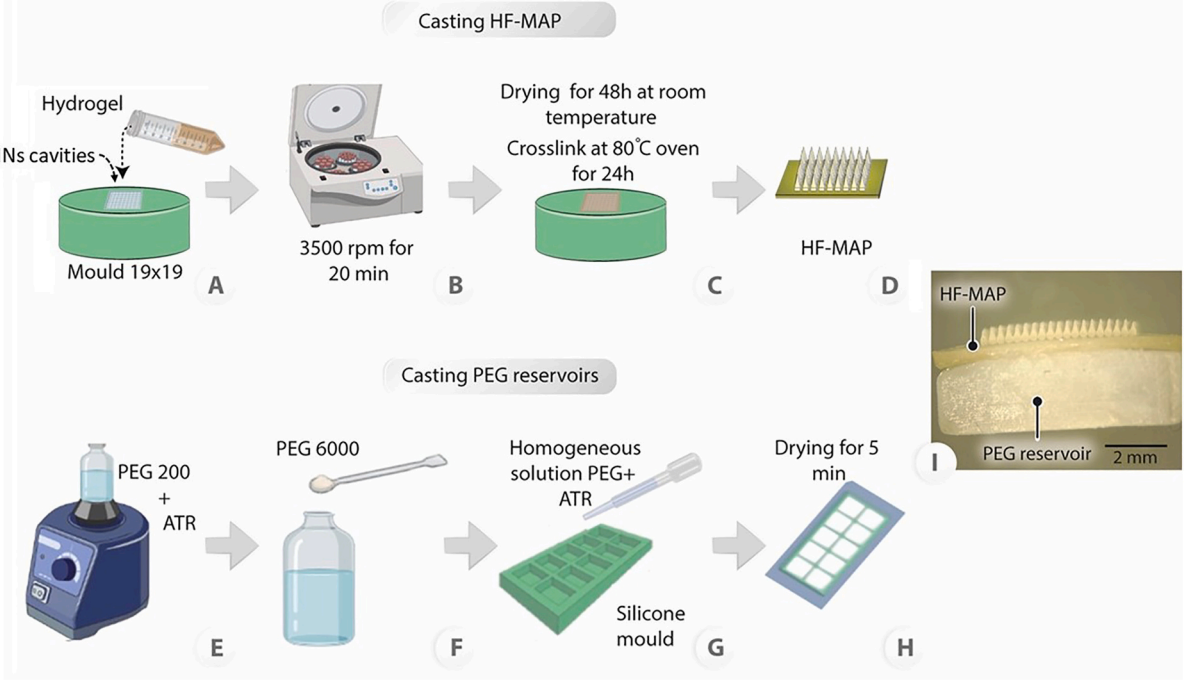

Fig. 2. Schematic representation showing (A-D) casting of HF-MAPs and (*E*-H) preparation of PEG reservoirs. (A) Hydrogel formulation cast into 19 × 19 moulds. (B) The blends are centrifuged at 3500 rpm for 20 min. (C) Moulds are left to dry for 48 h at room temperature, followed by a crosslinking step for 24 h at 80 °C. (D) Final crosslinked HF-MAP. (E) ATR is added to PEG 200, and they are vortexed until homogenous; they are heated at 80 °C until a clear solution is obtained. (F) PEG 6000 is added to the mixture, and they are placed back into the 80 °C oven for 15 min until the high MW PEG melts. (G) The mixture was vortexed to ensure homogeneity, cast in 1 cm^2 square silicone moulds and (H) left to dry for 5 min at room temperature. (I) The final product of HF-MAP and a PEG reservoir. The black scale bar resembles 2 mm in length.

Bethesda, MD, USA) [20,53,54].

2.2.3. Fabrication of hydrogel films

Hydrogel films were fabricated in a similar method to HF-MAPs. Briefly, aqueous blends were prepared using the formulations shown in Table 1. Following centrifugation for 5 min, aliquots of 500 mg of the hydrogel blends were slowly cast into 1 cm^2 square flat moulds. Then, they were centrifuged at 3500 rpm for 20 min to ensure that the gels were homogeneously distributed and to remove any surface bubbles that might affect the formulation. The cast moulds were then left to dry at room temperature for 48 h. After that, the films were demolded, and their sidewalls were cut using scissors. Subsequently, they were placed in an 80 °C oven overnight (24 h) to allow for crosslinking between the polymers by ester-bond formation [14].

2.2.4. Swelling studies of hydrogel-forming films in PBS (pH 7.4)

Films of each candidate formulation (1 cm^2) were weighed in the dry state, and their masses were recorded as m_0 (xerogels) at $t = 0$ (t_0). Afterwards, they were immersed in 40 mL of PBS at pH 7.4 for 24 h at room temperature. Films were removed at predefined time points, where the excess surface water was carefully dried using filter paper before recording their masses as m_t (hydrogels). The percentage of swelling was determined using Eq. 3.

$$Swelling\ (\%) = \frac{(mt - m0)}{m0} \cdot 100\% \quad (3)$$

The percentage equilibrium water content (%EWC) is used as an indicator for the maximum amount of water that can be potentially imbibed by a hydrogel sample, after which their masses will not differ. The %EWC was calculated using Eq. 4, where m_e represents the mass of swollen film at equilibrium and m_0 is the mass of film at the dry state.

$$\%EWC = \frac{(me - m0)}{m0} \cdot 100\% \quad (4)$$

2.2.5. Permeation of ATR across swollen hydrogel films

This experiment was conducted using hydrogel films. The quantity of ATR penetrating across swollen hydrogel films of candidate formulations was assessed using side-by-side diffusion cells (Permegear, Hellertown, PA, USA). This apparatus consisted of donor and receptor half-cell compartments and a 37 °C temperature-controlled water jacket. A magnetic stirring bar (4 mm × 10 mm) was used to agitate the solution in both compartments at 600 rpm. Before commencing the experiment, films were immersed in PBS (pH 7.4) for 24 h. Afterwards, they were cut into circles with a diameter of approximately 9 mm^2 using a stainless-steel blade to cover the gap between the donor and receptor compartments of the side-by-side cells. Each film was then sandwiched between the two half-cell compartments, and the interface was covered by Parafilm® M to prevent both leakage and evaporation of the release media. ATR was first dissolved in methanol and then diluted in PBS (pH 7.4) to obtain a solution of a final concentration of 1 $mg{\cdot}mL^{-1}$. An aliquot of 3 mL of this solution was added to the donor half-cell compartment. In the receptor half-cell, 3 mL of freshly prepared PBS (pH 7.4) heated and maintained at 37 °C was placed. At predefined time points of 0.5, 1, 2, 3, 4, 5, 6 and 24 h, the PBS from the receptor compartment was sampled and replaced with 3 mL fresh heated PBS to ensure sink conditions. All samples were then analyzed using RP-HPLC.

2.3. Formulation and characterization of PEG-based ATR reservoirs

2.3.1. Preparation of ATR-containing PEG reservoirs

A preliminary screening of cosolvent candidates, namely, PEG 200, PEG 400, and PEG 600, was performed. Excess amounts of ATR were placed in glass vials containing 5 mL of each cosolvent. The vials were then vortexed before being placed in a 37 °C shaking incubator at 40 rpm for 24 h. Afterwards, all samples were separately diluted in MeOH and then centrifuged at 14,800 rpm for 10 min. They were then diluted as needed, filtered using 0.2 μm Minisart® syringe filters and analyzed

using RP-HPLC.

The reservoir formulations were prepared using a solvent-melt SD method. PEG reservoirs were prepared using either PEG 6000 or PEG 8000 as a solid base and PEG 200 as a liquid cosolvent based on the results of the preliminary screening study. Different percentages of PEG 200 and PEG 6000 or 8000 were investigated as candidate formulations, as detailed in Table 2. ATR (8% *w*/w) was added to a glass vial containing PEG 200. It was first homogenized using a vortex and then heated for 10 min until ATR was completely dissolved, and a clear solution was obtained. Afterward, the required amounts of the higher MW PEG were weighed in separate glass vials. The corresponding quantity of ATR-containing PEG 200 solution was added to each vial according to the ratios described in Table 2. Samples were heated at 80 °C until complete dissolution of the higher MW PEG was achieved (~20 min). Later, they were vortex-mixed to ensure homogeneity before casting 250 mg of each formulation into 1 cm^2 square-shaped elastic silicone moulds to produce the reservoirs. After casting, the reservoirs were left at room temperature for 5 min to dry and solidify. Each reservoir of RF-1 and RF-3 contained 18 mg of ATR (7.2% *w*/w). However, 15 mg of ATR was successfully loaded in RF-2 and RF-4 (6% w/w), depending on the percentage of PEG 200 in each formulation. Fig. 2(*E*-H) displays a schematic representation of the steps required to prepare and cast ATR-containing PEG reservoirs, whereas Fig. 2I shows the final HF-MAP and RF-2 assembly.

2.3.2. Dissolution studies of ATR-containing PEG reservoirs

The dissolution time of all ATR-containing reservoir formulations was determined visually. Initially, the masses of the reservoirs were recorded at the dry state, and then each PEG reservoir was placed in glass vials containing 20 mL of 1% w/v sodium lauryl sulfate (SLS) in PBS (pH 7.4) preheated to and maintained at 37 °C. SLS (1% w/v) was added to the PBS in order to maintain sink conditions. This solvent was chosen based on the results of a preliminary saturation solubility study, which demonstrated its ability to enhance the solubility of ATR 20-fold compared to water (Fig. S1 in supplementary materials). Samples were agitated individually using magnet stirrers at 1500 rpm. The dissolution time was recorded in seconds.

2.3.3. Recovery percentages of ATR from solid PEG reservoirs

The recovery percentages of ATR from different formulations of ATR-containing reservoirs were evaluated. Reservoirs of each formulation were individually placed in 100 mL volumetric flasks containing 100 mL 1% w/v SLS in PBS at 37 °C and agitated using magnet stirrers at 1500 rpm. Upon their complete dissolution, samples were taken from each flask, filtered using 0.2 μm Minisart® syringe filters, diluted appropriately and analyzed using the validated *in vitro* RP-HPLC method. This facilitated the determination of the actual ATR content in each reservoir and, hence, the recovery percentage of ATR from the reservoirs.

2.3.4. TGA, DSC and FTIR studies

Pure ATR, pure excipients (blank reservoirs), and ATR-containing PEG reservoirs were studied in terms of thermogravimetric analysis (TGA), differential scanning calorimetry (DSC), and Fourier transform infrared (FTIR), using TGA Q50 and DSC Q100 (TA Instruments, Elstree, Hertfordshire, UK), and an attenuated total reflectance-Fourier transform infrared (ATR-FTIR) spectrometer (Accutrac FT/IR-4100™, Perkin Elmer, USA), respectively.

Table 2
The composition of the different formulations of PEG reservoirs.

Components	Composition (% w/w)			
	RF-1	RF-2	RF-3	RF-4
PEG 200	90	75	90	75
PEG 6000	10	25	–	–
PEG 8000	–	–	10	25

2.4. Ex vivo studies of HF-MAPs and PEG-based ATR reservoir assembly

2.4.1. Ex vivo permeation of ATR from SD PEG reservoirs

Franz diffusion cells were used in this study. Initially, skin samples were obtained from stillborn piglets, excised <24 h after birth, and carefully shaved using a razor. Afterwards, an electric dermatome trimmer (Integra Padgett® dermatome model B) was used to trim the shaved full-thickness skin to ~350 μm. The obtained dermatomed skin was then stored in a − 20 °C freezer until further needed. Before the experiment, the skin was pre-equilibrated in PBS pH 7.4 for 30 min until defrosted. Afterwards, it was carefully attached to the glass donor compartment of Franz cells using cyanoacrylate glue, with the epidermis side facing upwards. HF-MAPs from F2 and F4 were inserted using manual firm thumb pressure for 30 s. Pieces of dental wax wrapped with aluminum foil were used to support the insertion of the HF-MAPs. Subsequently, aliquots of 20 μL of 1% *w/v* SLS in PBS (release media) were added onto the top of the HF-MAPs before putting the drug reservoirs to promote the adhesion of the reservoirs to the MAP baseplates and to trigger their swelling. A 5 g stainless steel cylinder (diameter 11 mm, mass 11.5 g) was laid on the top of each HF-MAP- reservoir assembly to hold the set still and to prevent the expulsion of the swollen HF-MAPs from the skin. The receiver compartment contained 12 mL of the release media (1% w/v SLS in PBS), preheated, and maintained at 37 °C. The donor compartment was placed on top of the receiver compartment, and they were clamped and wrapped with Parafilm M® to prevent the evaporation of the release media. Control cells were also employed, where drug reservoirs were laid on top of the skin without the prior insertion of HF-MAPs. The aim was to compare ATR permeation across the skin from both setups. Samples of 200 μL were taken at predefined time points of 0.25, 0.5, 1, 2, 3, 4, 5, 6, 7, 8 and 24 h and were replaced with the same volume of fresh preheated release media. The samples were centrifuged at 14,800 rpm for 30 min, diluted when necessary and analyzed using RP-HPLC. The extraction of ATR from HF-MAPs, neonatal porcine skin and any remaining reservoir residues was performed at 24 h following the completion of the *ex vivo* study. This was achieved by first cutting the skin and HF-MAPs samples into small pieces before adding them into 2 mL microtubes containing 1.5 mL of methanol alongside two metal beads. The samples were then homogenized at 50 Hz using a Tissue Lyser LT (Qiagen, Ltd., Manchester, UK) for 20 min. The supernatant was then centrifuged at 14,000 rpm for 30 min before HPLC analysis. For ATR reservoir samples, 5 mL of methanol was added into glass vials containing the residuals of each drug reservoir. Vials were vortex-mixed until a clear solution was obtained. Next, 1.5 mL samples were taken from each glass vial, centrifuged at 14,800 rpm for 30 min, then appropriately diluted and analyzed using RP-HPLC.

2.4.2. Ex vivo skin deposition studies of PEG reservoirs

These studies were also conducted using a modified Franz diffusion cell setup. Full-thickness neonatal porcine skin (~0.5 mm thick) was used as a substitute for dermatomed skin to investigate the effect of skin thickness on the insertion and swelling of the HF-MAPs and their ability to deliver ATR. At two different sampling points of 4 and 24 h, HF-MAPs were removed. ATR was extracted from the skin, HF-MAPs, and the residuals of the drug reservoirs, as described previously, and analyzed using RP-HPLC. In another setup, and in order to investigate the distribution of ATR within the HF-MAPs and the skin layers, scanning electron microscope (SEM) was used. Following an *ex vivo* skin deposition study, HF-MAPs and skin samples were immediately frozen in a -80 °C freezer. Afterwards, they were placed in a freeze-dryer for 24 h to lyophilize them. They were then observed using the SEM.

2.5. In vivo delivery of ATR:

2.5.1. In vivo study design and execution

The *in vivo* study was conducted in accordance with the policy of the Federation of European Laboratory Animal Science Associations and the

European Convention for the protection of vertebrate animals used for experimental and other scientific purposes, with the 3Rs principles being followed (replacement, reduction, and refinement), under Project License PPL 2904, and Personal Licenses PIL 1892, PIL 1747 and PIL 2056. Female *Sprague Dawley* rats (total $n = 12$) (Charles River Laboratories, Harlow, UK), 8–10 weeks of age, possessing a mean weight of 266.3 ± 28.3 mg, were acclimatized to the animal house conditions for a week prior to the experiment. Animals were separated into two cohorts, each comprising 6 rats. Every 3 rats were housed in a separate cage. Each rat of the first cohort (rats 1–6) received an ATR suspension using an oral gavage at a dose of 40 mg.kg^{-1} (equivalent to 10 mg.rat^{-1}). The oral dose was selected based on a study published in 2019, where rats were given an oral dose of 10–80 mg.kg^{-1}·day with no reports of toxic reactions or side effects [55]. The oral suspension was prepared by dissolving the required mass of ATR in a 2% *w*/w PVA solution in water to produce a final suspension with a final concentration of 20 mg·mL^{-1}. The suspension was then mixed using SpeedMixer™ to ensure the homogeneity of the final product. This was freshly prepared in the morning immediately prior to its administration to the rats. The second cohort (rats 7–12) received four HF-MAPs combined with ATR reservoirs of RF-2. The dose given to each rat was approximately 60 mg.rat^{-1}.

To minimize the interference of the hair in the process of MAPs applications, the dorsal hair of the rats from the second cohort was removed prior to the experiment. Rats were formerly sedated using a gaseous anesthetic (2–4% *v*/v isoflurane in oxygen). The bulk hair was then shaved using electric hair clippers (Remington Co., London, U.K.). Afterwards, the remaining hair was removed by applying a depilatory hair removal cream (Boots Smooth Care hair removal cream sensitive, Boots, Nottingham, UK). Following this, rats were left for a 24 h period to allow their skin to recover, and to ensure the complete restoration of the skin's barrier function before inserting the MAPs [15]. On the following day, rats were sedated again using the same anesthetic gas, where HF-MAPs were inserted using firm thumb pressure onto a pinched section of skin on the back of the rats. An aliquot (10 μL) of water was applied to the center of the HF-MAPs, to promote the adhesion of the reservoir to the surface of the HF-MAPs and to trigger their swelling. Prior to their application onto the HF-MAPs, RF-2 reservoirs were initially secured inside the Microfoam™ adhesive frames (Fig. 3 A-B). The preparation steps of the Microfoam™ adhesive frames are shown in Fig. S3 in the supplementary materials. Afterwards, Tegaderm™ film was placed on top of the HF-MAPs, and kinesiology tape was eventually wrapped around the back of the rats to hold the MAPs and reservoirs assemblies firmly in place for 24 h (Fig. 3C). Four HF-MAPs and RF-2 reservoirs were applied to each rat. Each patch contained approximately 15 mg of ATR. Rats were housed individually for 24 h following the application of the patches to ensure that HF-MAPs and RF-2 drug reservoirs remained in their places. Fig. 3D shows the administration of an oral dose of ATR suspension using an oral gavage to rats of the control group.

Blood samples were collected into 1.5 mL preheparinized microtubes over 14 days *via* tail vein bleeds after ATR administration (either orally or using HF-MAPs). For the first day (day 0), samples from 4 different time points were obtained (1, 2, 4 and 6 h), and then sampling took place on day 1 (24 h), 2, 3, 4, 7, 10 and 14. Due to the restriction in blood sampling volumes required by the University's Institutional Project License, each rat was only allowed to be sampled twice per day. Therefore, to obtain samples at the 4 different time points on the first day, blood samples were taken from the first three rats in each cohort at the 2 and 6 h time points, whereas the other three animals were bled at 1 and 4 h. Afterwards, all animals ($n = 12$) were sampled at 24 h and thereafter for up to 14 days. On day 14, and upon the completion of the *in vivo* study, animals were sacrificed using carbon dioxide (CO_2) asphyxiation. To separate the plasma from the rest of the blood components, samples taken from rats were centrifuged immediately at 4900 rpm for 10 min at 4 °C. The obtained supernatants were then transferred into their respective labelled microtubes and stored in a − 20 °C freezer until further analysis (Fig. S4 in supplementary materials).

2.5.2. Preparation of ATR standards and ATR extraction from plasma

A stock solution of 1 mg·mL^{-1} ATR was originally prepared in MS-grade methanol. Afterwards, the stock solution was diluted in deionized water to obtain a standard with a final concentration range of 200 to 10,000 ng·mL^{-1}. Aliquots of 10 μL of each standard were added to microtubes containing 90 μL of plasma; then, they were vortex-mixed at 1500 rpm for 10 min, where a final calibration standard in a range of 20–1000 ng·mL^{-1} was attained. Thereafter, 300 μL of MS-grade methanol was added to each microtube containing ATR standard, followed by vortex-mixing for 25 min at 1500 rpm at room temperature. The samples were then centrifuged at 12,400 rpm for 10 min at 4 °C. Subsequently, supernatants were collected and transferred into polymeric feet inserts inside Agilent® vials, capped and stored in the freezer overnight prior to LC–MS/MS analysis. Five calibration curves were constructed over 3 consecutive days to validate the analytical method and ensure its reproducibility.

2.5.3. Sample preparation and ATR extraction from plasma

The extraction of ATR from plasma samples was performed by adding 300 μL of MS-grade methanol into aliquots of 100 μL of rat plasma in 1.5 mL microtubes. The mixture was vortexed for 25 min at 1500 rpm to allow for ATR extraction from plasma. Afterwards, the samples were centrifuged at 12,400 rpm for 10 min at 4 °C to precipitate the plasma proteins. Supernatants were then transferred to glass inserts with

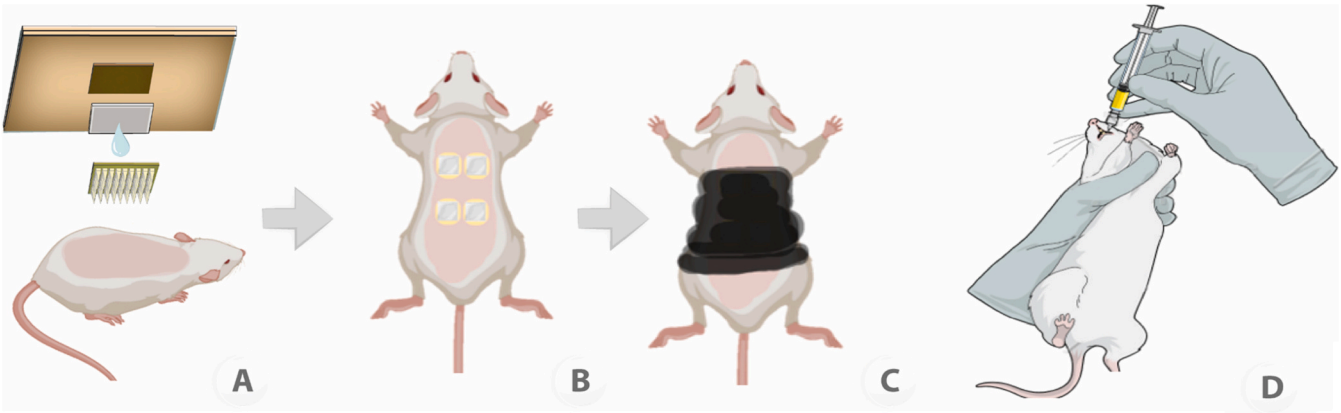

Fig. 3. Schematic representation demonstrating (A) the arrangement of HF-MAPs, drug reservoir and backing layer on the back of the rat, (B) the dorsal area of a rat after the application of 4 HF-MAPs, (C) the wrapping of kinesiology surgical tape around the back of a rat following HF-MAPs application, and (D) an oral gavage of ATR suspension being administered to a rat in the control group.

polymeric feet inside Agilent® vials prior to their bioanalysis using TQ-MS.

2.6. Pharmaceutical analysis of ATR

The *in vitro* quantification of ATR was performed using a reversed-phase HPLC Agilent 1220 series system (RP-HPLC), consisting of Agilent degasser G1312B, Agilent Binary pump SL G1312B, Agilent auto standard injector HiP-ALS SL G1367C, Agilent column thermostat TCC SL G1316B and Agilent Variable Wavelength Detector SL G1314C (Agilent Technologies Ltd., Stockport, UK). Based on a preliminary saturation solubility study, 1% *w/v* SLS in PBS (pH 7.4) was used to dilute the samples. The chromatograms were analyzed using Agilent ChemStation® Software B.02.01.

The separation and bioanalysis of the samples were carried out using an ACQUITY UPLC i-Class system, coupled to a Xevo TQ-MS (triple quadrupole MS/MS) mass spectrometer (Waters, Manchester, UK), using multiple reaction monitoring (MRM) (Waters, Manchester, UK). The system was operated in electrospray positive mode (ESI^+), and the transitions were initially obtained manually. The temperature of the ion transfer capillary was 250 °C, and nebulizer gas was 30 psi, dwell time per transition was 200 ms, gas flow 8 L/min, and collision gas 20. The quantification of ATR was accomplished by determining the peak area. Data processing was performed using Mass Lynx® Software system. Table 3 summarizes the parameters used in the ATR analysis both *in vitro* and *in vivo*.

2.7. Pharmacokinetic analysis

Noncompartmental pharmacokinetic analysis (PK analysis) for plasma concentrations of ATR was conducted using PK Solver as an add-in tool to Microsoft® Excel (Microsoft Corporation, Redmond, WA, USA). Drug concentrations ($ng{\cdot}mL^{-1}$) were plotted against time (days). The maximum plasma concentration (C_{max}) of ATR and the time of the maximum concentration (T_{max}) were directly obtained by inspecting the raw data. Other parameters, including AUC from time zero ($t = 0$) to the last experimental time point ($AUC_{0–14}$), AUC from time zero ($t = 0$) until infinity ($AUC_{0\text{-inf\_obs}}$), and mean residence time (MRT), were all determined. The area under the curve ($AUC_{0–14}$) was calculated using the linear trapezoidal method, from t = 0 (at the start of the experiment) until $t = 14$ days (the last experimental time point).

Table 3
Summary of the *in vitro* and *in vivo* analysis methods.

Method	RP-HPLC for *in vitro* samples	TQ-MS for *in vivo* samples (rat plasma)
Column	Phenomenex SphereClone® C-18 (ODS1) column: 150 mm × 4.6 mm internal diameter, 5 μm packing	Zorbax Eclipse XDB C-18 column: 50 mm × 4.6 mm internal diameter, 1.8 μm packing
Temperature	30 °C	40 °C
Mobile phase composition	Phosphoric acid solution at pH = 2.1 (A) and methanol (B), 40%: 60% *v/v*	0.1% v/v formic acid in water at pH 2.1 (A), and acetonitrile (B), using a gradient: 30% A: 70% B (0–2.5 min) 5% A: 95% B (2.6–3.6 min) 30% A: 70% B (3.6–5 min)
Range	0.125–50 $\mu g{\cdot}mL^{-1}$	20–1000 $ng{\cdot}mL^{-1}$
Flow rate (mL/min)	1	0.5
Injection volume (μL)	30	5
Detector	UV detection at 240 nm	TQ-MS mass spectrometer using MRM detection, precursor ion 559.45 *m/z* and base fragment ion 446.35 *m/z*
Retention time	5.2 min	1.54 min
LOQ	1 $\mu g{\cdot}mL^{-1}$	20 $ng{\cdot}mL^{-1}$

2.8. Statistical analysis

All data presented in this article were stated as means ± S.Ds. The least squares linear regression analysis, correlation analysis, LOD and LOQ were all performed using Microsoft® Excel 2010 (Microsoft Corporation, Redmond, USA). All statistical analyses were performed using GraphPad Prism® version 9 (GraphPad Software, San Diego, USA). The normality of the data obtained was initially assessed using the Shapiro–Wilk test. If the p value calculated from the test was >0.05, the data were assumed to be normally distributed. For normally distributed data (parametric data), an unpaired t-test was performed to analyse two groups, one-way analysis of variance (ANOVA), and two-way ANOVA with Tukey's *post hoc* test were used to analyse the differences among separate groups (≥ 3 groups). Statistical significance was represented by $p < 0.05$ in all cases.

3. Results and discussion

3.1. Development and characterization of HF-MAPs

Once crosslinked and their sidewalls were removed using a heated blade, HF-MAPs were visualized using a Leica EZ4D light stereomicroscope (Leica Microsystems, Milton Keynes, UK) and a scanning electron microscope TM3030 (Hitachi, Krefeld, Germany). Four hydrogel formulations were initially investigated. Digital images using the light microscope and SEM of formed HF-MAPs from the two lead formulations (F2 and F4) are displayed in Fig. 4(A-D).

3.1.1. Assessment of the mechanical properties of HF-MAPs

The percentage in height reduction of HF-MAPs was assessed as an indicator of their mechanical robustness to assure that HF-MAPs can withstand the pressure when applied to the skin and will not break [56]. Fig. 4E shows the heights of the HF-MAPs of the four distinct formulations before and after applying 32 N per patch force using a TA. XT2 Texture Analyzer (Stable Micro Systems Ltd., Godalming, UK). This force was chosen as it resembles the mean human thumb force as previously reported [53]. For F1, F2, F3, and F4, the height reduction percentages were 13.66%, 7.79%, 11.56%, and 4.47%, respectively. The exertion of the 32 N force could significantly ($p < 0.05$) reduce the MNs heights of F1 and F3, as shown in Fig. 4E. F2 and F4, on the other hand, exhibited the lowest percentage of height reduction, with no significant difference in height before and after the test ($p > 0.05$). HF-MAPs from all formulations were sturdy; they were hard in nature yet not brittle, indicating their robustness once inserted into the skin [11].

3.1.2. Evaluation of HF-MAP insertion properties in vitro and ex vivo

The HF-MAP insertion properties were first investigated *in vitro* using Parafilm® M as a validated skin-simulant artificial membrane [53], and then *ex vivo,* using excised neonatal porcine skin. The results in Fig. 4H show that all HF-MAPs formulations could completely penetrate the first two layers of the Parafilm® M stack. However, their insertion into the third layer, with a depth of 378–507 μm, varied insignificantly ($p > 0.05$). This insertion depth represents nearly 84% of the total needle height, which is similar to the data previously reported in the literature [21,57,58]. The thickness of the epidermis is approximately 100–150 μm, while the dermis is 0.5–5 mm thick, depending on the body site [59–61]. Therefore, it is valid to presume that all four HF-MAPs can penetrate the skin's dermal layers. Since this region is non-innervated, HF-MAP technology allows for painless delivery of molecules across the skin, which is a significant advantage over using a needle and syringe platform [11]. The heights of the four formulations were measured before and following their insertion into the Parafilm® M layers. The results are shown in Fig. 4G and demonstrate no significant difference in the heights of HF-MAPs before and after their insertion, which could further emphasize their safety upon their insertion into human skin.

Despite the comparability in their insertion profile and mechanical

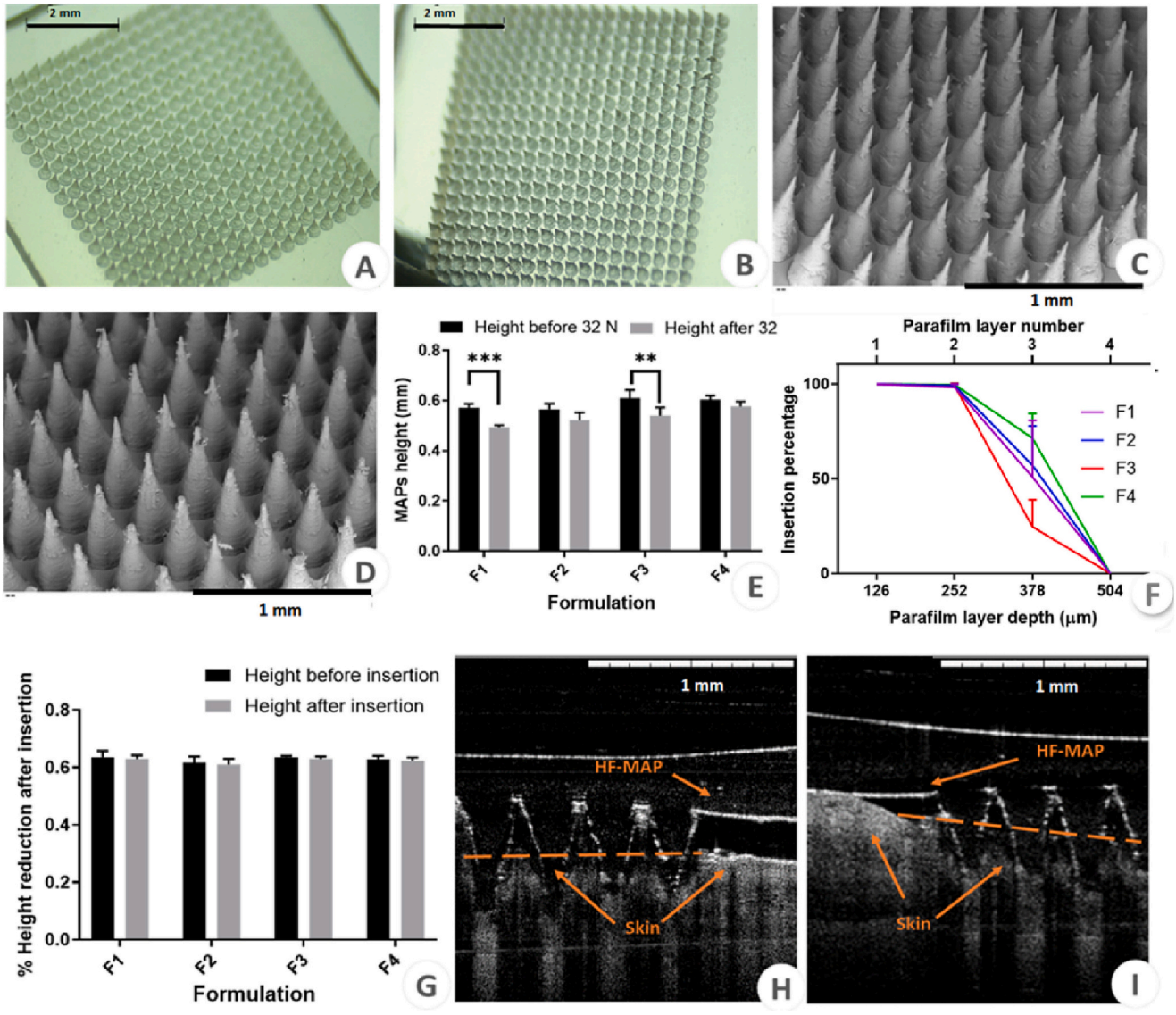

Fig. 4. Summarizes the mechanical characterization of HF-MAPs. Digital microscopic images of (A) F2 HF-MAP and (B) F4 HF-MAP using a light microscope, where the black scale bar resembles a length of 2 mm. (C) SEM images for F2 and (D) F4 HF- MAPs, where the length of the black scale bar = 1 mm. (E) Heights of HF-MAPs before and after the application of 32 N force for 30 s against a stainless-steel baseplate. (Means + S.Ds., $n = 3$) (**$p = 0.0012$, ***$p = 0.0003$). (F) Percentage of holes created in each Parafilm® M layer and approximate insertion depth of each formulation of HF-MAPs. (Means ± S.Ds., n = 3). (G) Height reduction of MAPs before and after their insertion into the Parafilm® M sheet using a 32 N force for 30 s. (Means + S.Ds., $n = 4$). Representative OCT images of hydrogel-forming MAPs prepared from (H) F2 and (I) F4, where the white scale bar represents a length of 1 mm.

properties, and in contrast to the other three formulations, F1 HF-MAPs was excluded from further studies. This was due to bubble-formation on their surfaces, which led to the wastage of many HF-MAPs during the manufacturing phase. Bubble-formation could be attributed to the high percentages of both Gantrez® S-97 (20% *w*/w) and PEG 10,000 (10% w/w) in the hydrogels. This could have increased the viscosity of the formulation [62].

The *ex vivo* insertion studies were performed using excised full-thickness neonatal porcine skin (~0.5 mm thick). The insertion depth of HF-MAPs from formulations F2 and F4 into porcine skin was then visualized using an optical coherence tomography (OCT) microscope (EX1301 VivoSight®, Michelson Diagnostics Ltd., Kent, UK), as shown in Fig. 4(H—I). HF-MAPs displayed insertion depths of 451.4 ± 11.3 μm and 455.4 ± 6.6 μm for F2 and F4, respectively ($p > 0.05$).

3.1.3. Evaluation of the swelling properties of HF-MAPs

The swelling capacity of hydrogels is of utmost importance, as it can potentially affect their mechanical characteristics and solute diffusion capacity [63]. Throughout 24 h, the swelling kinetics of three distinct Gantrez® S-97-based films, namely, F2, F3, and F4, were examined, as shown in Fig. 5A. Due to the substantial bubble development during its manufacturing, F1 was not chosen for further exploration in this study. Fig. 5B shows the swelling profiles of the three formulations, with F4 demonstrating a significant superiority ($p < 0.05$) in swelling capacity over F2 and F3, starting from 15 min until 24 h. The swelling percentage of F4 after 30 min of immersion in PBS (pH 7.4) was approximately 1000%, as shown in Fig. 5B. On the other hand, the swelling percentages of F2 and F3, at the same timepoint, were 434% and 326%, respectively. The swelling of hydrogels is mainly governed by their crosslinking degree, polymer, and crosslinker type [23,25]. The crosslinking ratio can be defined as the molar ratio between the crosslinking agent and polymer backbone units [25]. As the crosslinking density of hydrogels increases, their ability to swell decreases [64]. Once the modifying agent Na_2CO_3 was added to the F4 HF-MAPs formulation, a significantly ($p <$

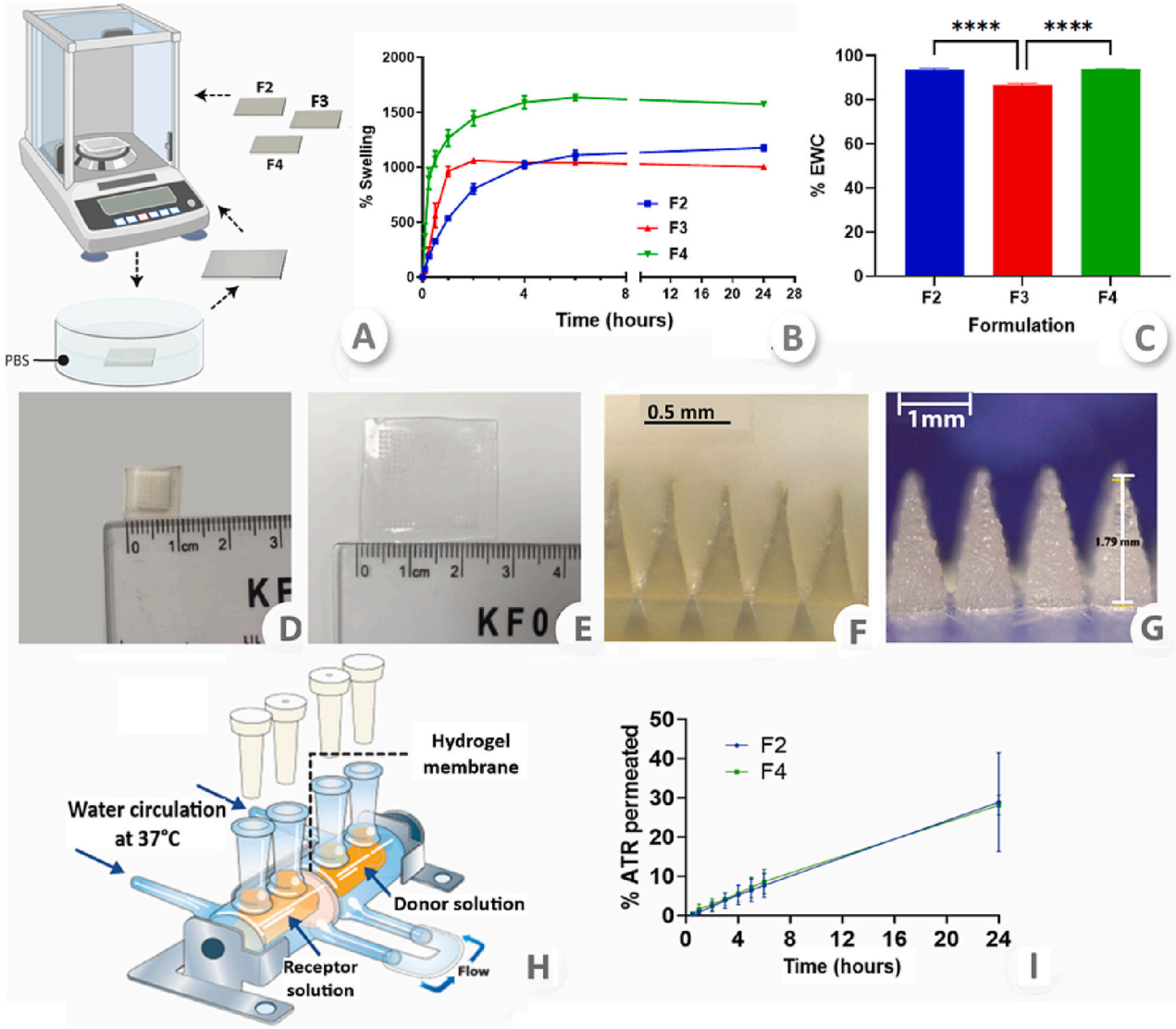

Fig. 5. Demonstrates the swelling of HF-MAPs and its effect on the permeation of ATR. (A) Swelling study setup, where films from the 3 different hydrogel formulations (F2, F3, F4) were weighed at $t = 0$ and at predefined timepoints following their immersion in PBS (pH 7.4) to study their swelling behavior. (B) The swelling kinetics of F2, F3 and F4 Gantrez® S-97-based hydrogel films in PBS (pH 7.4). (Means ± SDs., $n = 3$) and (C) The %EWC of hydrogel films from F2, F3 and F4. (Means +SDs., n = 3) (****$p < 0.0001$). (D-E) HF-MAPs of the F4 'super swelling' formulation (D) before and (E) after their swelling in PBS pH 7.4 over 24 h. (F-G) Microscopic images of F4 HF-MAPs (F) before swelling and (G) following its immersion in PBS for 24 h. (H) Side-by-side apparatus used in the permeation study. (I) The percentage of ATR permeated across the swollen hydrogel films of F2 and F4 over24 h. (Means ± SDs., n = 3).

0.05) higher swelling capacity was observed. This can be attributed to the interaction between Na_2CO_3 and the COOH moiety in Gantrez® S-97, forming the sodium salt of the free acid, and thus preventing ester-based crosslinking. This can result in a lower crosslinking density along with a higher swelling percentage. A proposed crosslinking mechanism between Gantrez® S-97 and PEG 10,000 and a salt-formation reaction between Gantrez® S-97 and Na_2CO_3 is presented in Fig. S2 in the supplementary materials. Furthermore, the addition of the sodium carbonate would probably raise the pH of the hydrogels, thus causing more COOH groups to ionize to COO-, preventing them from interacting with the OH groups in PEG to form esters. These swelling results are comparable to similar findings in the literature [12,29,65,66]. The esterification reaction, previously described by Donnelly *et al* in 2014, resulted in the new ester bond formation of sodium salts on free carboxylic acid groups, which was seen in the FTIR spectra of the 'super swelling' formulation at 1500–1600 cm^{-1} [12]. This band was unique due to its absence in the spectra of the other formulations [12]. As a marker of the water uptake capability of formulations, the percentage equilibrium water content (%EWC) was determined. The %EWC findings, shown in Fig. 5C, followed a similar pattern to the results of the swelling study. The presence of Na_2CO_3 in F4 resulted in a lower crosslinking density, and thus, a significantly ($p <$ 0.0001) higher %EWC. Fig. 5(D-G) depicts a 'super swelling' F4 HF-MAP before and after 24 h of immersion in PBS at pH 7.4. The swelling percentage of F3 from 2 h onwards underwent gradual decrements. This could be due to its lower content of Gantrez® S-97. Furthermore, F2 and F4 possessed significantly higher %EWC. Therefore, subsequent studies were conducted using F2 and F4 HF-MAPs.

3.1.4. *In vitro permeation of ATR through swollen hydrogel films*

The quantity of ATR permeating across swollen hydrogel films of F2 and F4 HF-MAPs was assessed using side-by-side diffusion cells (Permegear, Hellertown, PA, USA), as shown in Fig. 5H. ATR permeation profiles across the swollen hydrogel films of formulations F2 and F4 at equilibrium are presented in Fig. 5I. ATR permeation profiles through both membrane formulations exhibited a remarkably similar pattern,

with no significant difference denoted between both formulations ($p > 0.05$) at any time point. After 24 h, a cumulative amount of 867.1 ± 377.6 μg and 843.8 ± 76.2 μg of ATR could permeate across swollen films of F2 and F4, respectively. This amount stands for approximately 28.9 ± 12.6% for F2 and 28.1 ± 2.5% for F4 of the initial ATR amount loaded in the donor half-cell of the setup. This could be attributed to the fact that both film formulations prepared from Gantrez® S-97 could have been beneficial in enhancing the permeation of hydrophobic ATR due to their characteristics of high water-containing capacity and high porosity within the hydrogel formulations. Therefore, the mobility of ATR molecules could have been less restricted within the hydrogel network [67]. However, the amount of ATR recovered from the donor half-cell at the end of the study was 1258 ± 158.5 μg from F2 and 1819.2 ± 181.3 μg from F4, representing approximately and 42 ± 5.8% and 60.6 ± 6% of the original drug loading, respectively. This means that approximately 30% of ATR was entrapped in the swollen film of the F2 formulation compared to approximately 12% in F4. This is due to the higher crosslinking density of F2, hindering ATR diffusion and resulting in entrapping a higher percentage of the drug within the swollen hydrogel compared to F4. Nonetheless, both formulations were further evaluated in subsequent *ex vivo* studies.

3.2. Formulation and characterization of PEG-based ATR reservoirs

One of the most crucial factors affecting the absorption of drugs is their dissolution [68]. It plays a vital role in achieving therapeutic effects following drug administration. However, >40% of commercially available drugs are hydrophobic molecules, exhibiting poor aqueous solubilities, thus resulting in low bioavailability and high variability in the concentration of drugs in the blood due to suboptimal delivery [35]. ATR is a class II drug according to the BSC classification [51,52], possessing high permeability and low aqueous solubility (0.1 mg·mL^{-1}) [51,69]. One of the commonly used approaches to overcome the limitation of drug dissolution, and thus bioavailability, is the use of SD as a solubility enhancing technique [39]. As the HF-MAPs themselves are devoid of any drug, the formulator can control the drug release rate.

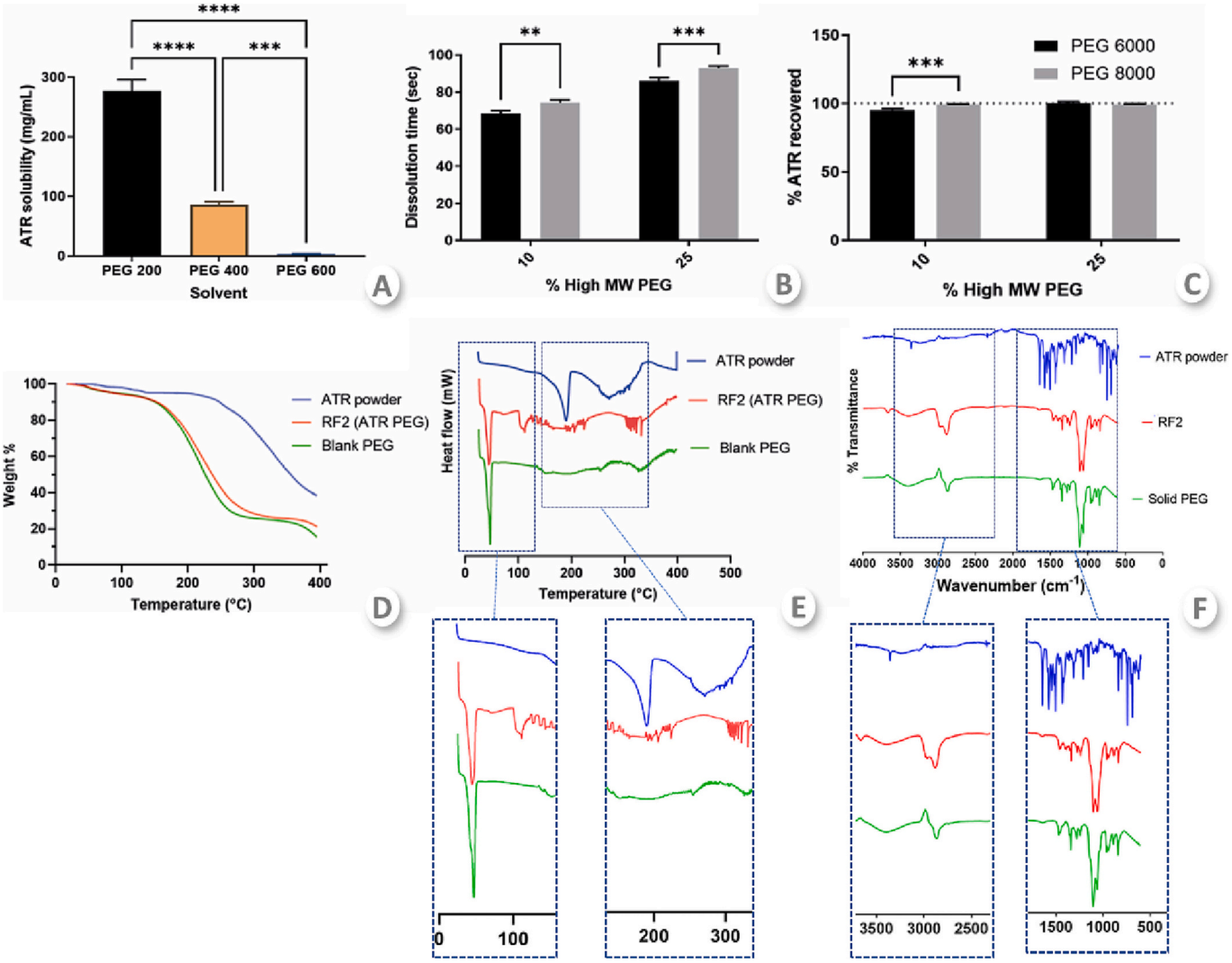

Fig. 6. Shows the characterization of ATR-based SD reservoirs. (A) The saturation solubility of ATR in a range of different low molecular weight PEG, namely, PEG 200, PEG 400, and PEG 600. (Means + S.Ds., $n = 3$) (***$p = 0.0003$, ****$p < 0.0001$) (B) Dissolution time (in *sec*) of ATR-containing reservoirs after being placed in 20 mL of 1% *w/v* SLS in PBS, preheated to 37 °C, and stirred at 1500 rpm using a stirring bar. (Means + S.Ds., n = 3) (***$p = 0.0008$, **$p = 0.0021$). (C) Percentage ATR recovered from drug reservoirs of each different formulation. The formulations tested were RF-1, RF-2, RF-5, and RF-6 due to their significantly shorter dissolution time. (Means + S.Ds., n = 3) (*** $p = 0.0006$). (D) Representative TGA thermograms of pure ATR powder, the selected PEG reservoir formulation (RF-2), and the physical mixture of blank solid PEG 200 and PEG 6000. (E) Representative DSC thermograms of pure ATR powder, the selected PEG reservoir formulation (RF-2), and the physical mixture of blank solid PEG 200 and PEG 6000. (F) Representative FTIR spectra of pure ATR powder, the selected PEG reservoir formulation (RF-2), and the physical mixture of blank solid PEG 200 and PEG 6000.

Therefore, polymer selection plays a critical role in drug delivery. In this study, an SD approach using the solvent-melt method was applied in developing PEG reservoirs as hydrophilic carriers for the delivery of hydrophobic ATR, upon its combination with HF-MAPs, across the skin. Several studies demonstrated that the presence of PEG in a formulation could improve the solubility of various drugs [42,44,48,70]. PEGs can increase the wettability of hydrophobic molecules, thus improving their solubility [47,71]. In addition, PEG possesses an established safety profile. They are also of a low cost, tend to be well-tolerated, and can be easily scalable to an industrial level in the future [70,72]. Therefore, they were selected as the matrix for the preparation of the ATR-containing SD reservoirs.

3.2.1. Dissolution studies

The results of the preliminary saturation solubility study of ATR in PEG 200, PEG 400, and PEG 600, as candidate cosolvents in the preparation of the SD, are presented in Fig. 6A. The saturation solubility of ATR in PEG 200 was 277.4 ± 18.8 mg·mL^{-1}. This was significantly ($p < 0.05$) higher than the saturation solubilities of ATR in both PEG 400 and PEG 600, which were 86.4 ± 4.9 mg·mL^{-1} and 3.62 ± 0.4 mg·mL^{-1}, respectively. This can be ascribed to the dielectric constant of the low-MW PEG, as it is also directly proportional to the polarity of the solvent used [73]. The dielectric constants of PEG 200, 400 and 600 at 35 °C were reported to be 17.5, 12.5 and 9.6, respectively [73]. Furthermore, lower MW PEGs possess shorter hydrocarbon chains; thus, as the MW of PEG increases, the length of the hydrophobic chains will also increase and result in a shift from hydrophilic to amphiphilic properties [74]. Therefore, PEG 200 was used as the cosolvent of choice to prepare PEG reservoir formulations.

PEG reservoirs were prepared in an SD technique, using either PEG 6000 or PEG 8000 as a solid base and PEG 200 as a liquid cosolvent, based on the results of the preliminary screening study. As per the dissolution time of ATR-containing PEG reservoirs, the results are presented in Fig. 6B. Due to their high PEG 200 content, reservoirs from all formulations were entirely dissolved within 2 min. Statistically, as the content of PEG 200 increased in the system, the dissolution time was significantly ($p < 0.05$) shorter. This is potentially due to increased hydrogen bonding between the polar hydroxyl groups of PEG and the dissolution media, resulting in enhanced wettability and reduced interfacial tension [47,71,74]. According to Fig. 6C, ATR recovery percentages from all ATR-containing PEG reservoirs were between 95 and 100.2% of the theoretical content of ATR initially loaded. This finding confirms the stability of ATR within the reservoirs and the absence of any compatibility issues between ATR and PEG.

Considering the previous results, and despite the higher content of ATR in those reservoirs, RF-1 and RF-3 were eliminated as formulation candidates. RF-1 and RF-3 incorporated 90% PEG 200 into their formulation. Therefore, they were prone to form droplets on their surfaces shortly following casting due to their high liquid content (Table S1 in supplementary data). RF-2 and RF-4, on the other hand, were given further consideration, as they showed a greater integrity at ambient temperatures after 2 h of casting. This granted those formulations with more favorable qualities and appearance, potentially making them more appealing to patients. Furthermore, as demonstrated in Fig. 6B, the dissolution time of RF-2 was significantly less than that of RF-4 ($p = 0.0008$). Therefore, RF-2 was anticipated to provide earlier and faster dissolution during the *ex vivo* permeation and skin deposition studies.

3.2.2. Thermal analysis and ATR-FTIR spectroscopy studies

Thermal gravimetric analysis (TGA) was conducted to assess the thermal behavior of ATR upon its incorporation into the lead PEG reservoir formulation (RF-2), by analyzing the water content in the samples. Fig. 6D shows TGA thermograms of samples containing pure ATR powder, a blank PEG reservoir, and the ATR-containing PEG reservoir of choice (RF-2). The results revealed that the thermograms of both the RF-2 and blank PEG reservoirs followed a similar trend, with approximately 5% weight loss observed before reaching 100 °C. This can be ascribed to the evaporation of excess water adsorbed on the surface and embedded within the formulation. At temperatures ranging from 150 to 300 °C, significant weight loss was recorded, accounting for more than half of the reservoir mass (Δm = 62.2% for RF-2 and 64.3% for blank PEG reservoir), potentially indicating thermal decomposition of the formulation. The pure ATR powder was thermally stable up to 200 °C. Nonetheless, between 250 and 400 °C, an abrupt decrease in ATR mass was observed, where Δm was 56.5%. These findings are similar to the results reported in the literature [75].

Differential scanning calorimetry (DSC) was used to determine the heat and temperature of the transformation of the samples. DSC thermograms of the different samples are presented in Fig. 6E. At approximately 158.4 °C, an endothermic peak of the crude ATR powder was noticed, which corresponds to the melting point of ATR at 159.14 °C [76]. This peak was absent in the RF-2 thermogram, which could suggest the conversion of ATR from a crystalline into an amorphous form. A sharp endothermic peak at approximately 46.9 °C was seen in the blank PEG thermogram, corresponding to the melting point of PEG 200 and PEG 6000. A similar peak was also identified in the RF-2 thermogram at 44 °C. The presence of such comparable peaks may be evidence of SD formation.

Drug-carrier interactions can often lead to significant changes in the Fourier transform infrared (FTIR) profiles of S.Ds. The RF-2 spectrum was compared to the spectra of both ATR powder and a blank PEG reservoir, as presented in Fig. 6F, where the presence and absence of characteristic peaks linked with specific structural characteristics of ATR were observed. Five characteristic signals can be observed in the ATR powder spectrum (peak energies: 3366 cm^{-1} for an-OH stretching, 3228 cm^{-1} for -NH bending, 1652 cm^{-1} for -C=O stretching, 2904 cm^{-1} for -CH (aromatic) stretching, and 1595 cm^{-1} for C=C (aromatic) stretching. The spectra of RF-2 exhibited a remarkable shift compared to the ATR powder spectrum. Nevertheless, those new bands had similar peak energies to the characteristic bands of the blank reservoir, as they were present in both spectra. This can be ascribed to the development of interparticle bonding between ATR and PEG [77]. The RF-2 FTIR spectra show overlapping of O—H and N—H groups (at 3366 and 3228 cm^{-1}, respectively) and broadening of the peak. However, the remaining peaks related to C—H, C—O, and C—N stretching remained unaffected, suggesting no notable change in the overall molecular symmetry [78]. There is also the possibility that PEG might form hydrogen bonds with itself (PEG-PEG bonds). Therefore, high energy might be initially required to break those PEG-PEG bonds and to help form new bonds with ATR [79].

3.3. Ex vivo studies of HF-MAPs and PEG-based ATR reservoir assembly

3.3.1. Ex vivo permeation study using the HF-MAP/PEG-based ATR reservoir assembly

For the *ex vivo* permeation studies, modified Franz diffusion cells (Permegear, Hellertown PA, USA) (Fig. 7A) were used to evaluate the amount of ATR capable of permeating through the dermatomed neonatal porcine skin, as a human skin simulant, using HF-MAPs. Fig. 7B depicts the *ex vivo* permeation profiles of ATR from RF-2 PEG reservoirs through F2 and F4 HF-MAPs. The profiles of both formulations followed a similar trend to their swelling profiles. At every time point starting from 2 h onwards, a significantly higher quantity of ATR was delivered *via* F4 HF-MAPs compared to F2 ($p = 0.0018$) and the control setup ($p = 0.0001$). Approximately 2.05 ± 0.23 mg of ATR was delivered and quantified in the receiver compartment of Franz cells after 24 h upon using F4 HF-MAPs. A significantly lower quantity ($p < 0.05$) of only 0.64 ± 0.37 mg was delivered using F2 HF-MAPs. This was expected due to the lower crosslink density of F4 HF-MAPs, which could have led to less drug entrapment within the system. In contrast, given the lower swelling capacity of F2 HF-MAPs, insufficient hydration led to their failure to thoroughly dissolve ATR reservoirs during the *ex vivo* study.

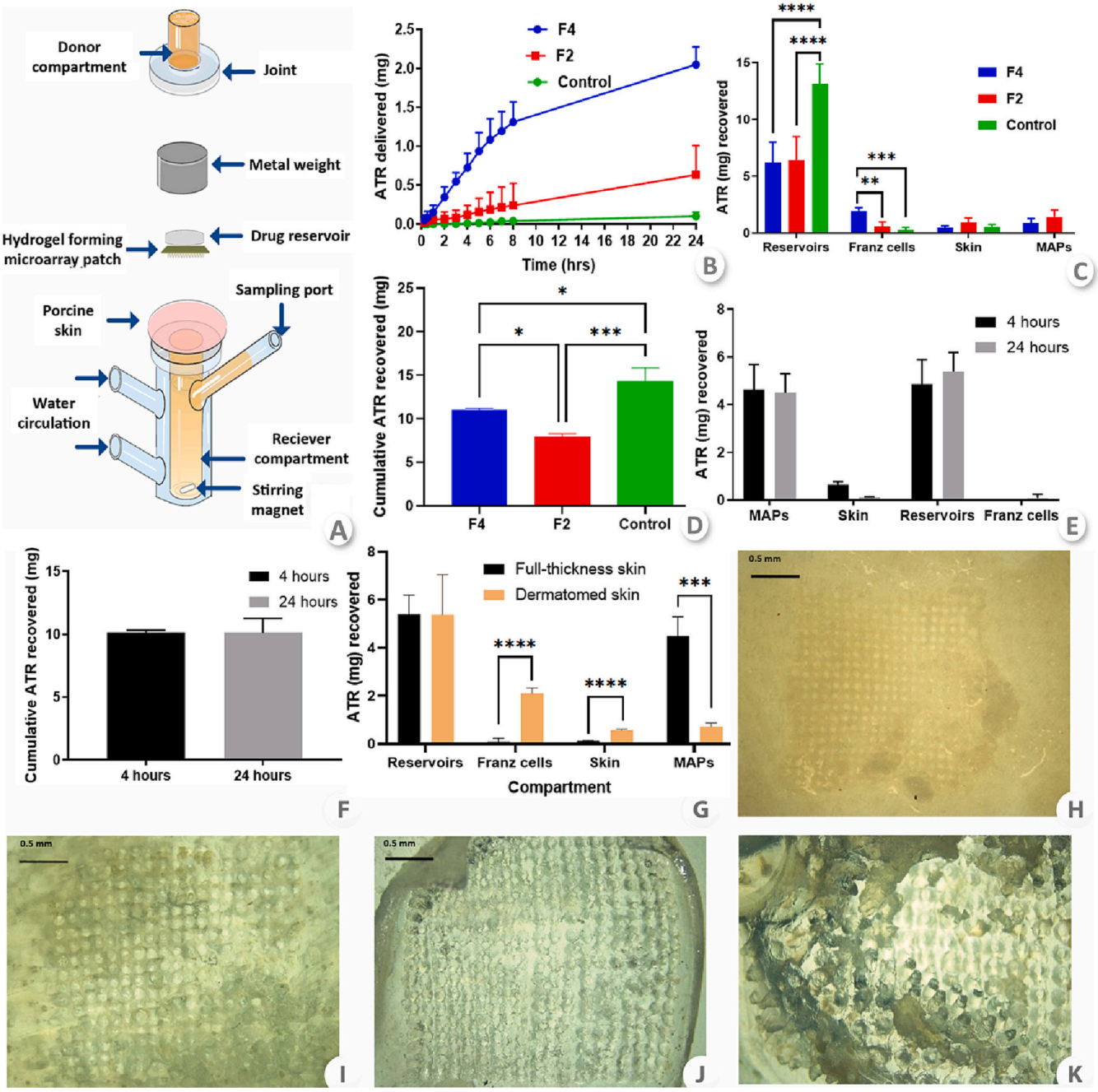

Fig. 7. Illustrates the *ex vivo* permeation and skin deposition studies using Franz diffusion cells. (A) A schematic representation of the Franz cell setup. (B) *Ex vivo* permeation profiles of ATR from PEG reservoirs of the selected formulation (RF-2), in combination with super swelling HF-MAPs (F4) and normal swelling HF-MAPs formulation (F2), and control cells that contained no HF-MAPs across dermatomed neonatal porcine skin over 24 h. (Means + S.Ds., $n \geq 4$). (C) The quantity of ATR in mg recovered from each compartment of F4 and F2 HF-MAPs setups and the control setup. (Means + S.Ds., $n \geq 3$) (****$p < 0.0001$, ***$p = 0.0001$, **$p = 0.0018$). (D) Cumulative amount of ATR recovered from each Franz cell setup following the conclusion of the experiment. (Means + S.Ds., $n = 3$) (***$p = 0.0004$, *$p < 0.02$). (E) The quantity of ATR in mg recovered from each compartment following skin deposition studies for 4 and 24 h. (Means + S.Ds., n = 3). (F) Cumulative amount of ATR recovered from each Franz cell set following skin deposition studies for 4 and 24 h, respectively. (Means + S.Ds., n = 3). (G) Comparison of the amount of ATR (mg) retrieved from each compartment for both full-thickness and dermatomed skin setups. (Means + S.Ds., $n \geq 3$) (****$p < 0.0001$, ***$p = 0.0002$). (H) Digital microscope images displaying porcine skin following initial removal of F4 HF-MAPs after 8× magnification after 4 h, where full penetration of the HF-MAPs arrays into the porcine skin can be observed. (I) Digital microscopic image showing the porcine at 24 h upon the removal of F4 HF-MAPs, where full insertion is seen in the image. (J) Digital microscopic pictures representing F4 HF-MAPs at 8× magnification after 4 h. (K) Digital microscopic picture representing F4 HF-MAPs at 8× magnification after 24 h, where the HF-MAPs were observed to had swollen more extensively as they remained in the skin for 24 h rather than 4 h.

Nevertheless, only 0.23 ± 0.22 mg of ATR was detected in the receiver compartment in control cells where no HF-MAPs were used. This can also show that HF-MAPs can significantly enhance the amount of ATR delivered transdermally. It was also apparent that the drug permeation increased linearly over the first 8 h, followed by slow increments in the cumulative drug concentration. However, ATR permeation, especially from F4 HF-MAPs, did not reach a plateau, suggesting that it may potentially be continued for durations longer than 24 h. Nevertheless, due to the nature of the Franz cell setup and the use of excised porcine skin at 37 °C, permeation for longer than 24 h could not be evaluated in

this case.

After 24 h, all Franz cells were disassembled, and ATR was extracted from the skin, HF-MAPs, and the residues of the drug reservoirs from each Franz cell to quantify ATR found in each compartment after concluding the experiment. It was found that ATR reservoirs from the control setups maintained a very similar size and shape to the original reservoirs, whereas in the HF-MAPs-containing setups, reservoirs were dissolved, as shown in Fig. S5 in the supplementary materials. A mean of 13.12 ± 1.73 mg of ATR was quantified from the reservoir residuals in the control setup, which was significantly ($p < 0.0001$) higher than the quantity recovered from the reservoirs of both HF-MAP-containing setups. On the other hand, the amount of drug reckoned from the residuals of the F4 and F2 HF-MAPs setup reservoirs was 6.2 ± 1.82 mg and 6.44 ± 2.06 mg, respectively. Moreover, there was no significant difference between the amounts of ATR recovered from either skin or HF-MAPs samples from all setups, as they were similar ($p > 0.05$). The amount of ATR retrieved from Franz cells was significantly higher upon using F4 HF-MAPs compared to the F2 HF-MAPs formulation ($p = 0.0018$) and the control group ($p = 0.0001$). Fig. 7C summarizes these findings.

The cumulative amount of ATR recovered from all Franz cell compartments was calculated for each setup individually. This was mainly performed to estimate the percentage of ATR recovered from the total amount initially loaded per reservoir. A mean of 11.0 ± 0.14 mg ATR was recovered from the samples obtained from the F4 HF-MAPs-containing setup, which represents approximately 79.28% of the initial ATR loading. Additionally, a mean of 7.96 ± 0.42 mg was quantified from the F2 HF-MAP-containing setup, which is equivalent to 57.58% of the initial drug load. However, 13.55 ± 1.06 mg ATR was recovered for the control (no HF-MAPs) setup, accounting for 98.01% of the ATR initially loaded in the reservoirs. These results are represented in Fig. 7D.

3.3.2. Ex vivo skin deposition studies

Franz-cells were again employed to assess the amount of ATR deposited in full-thickness excised neonatal porcine skin using the F4 HF-MAPs formulation with RF-2 PEG-based SD reservoirs at two predefined time points: 4 and 24 h. In this instance, HF-MAPs were not capable of completely penetrating through the skin due to its higher thickness. Consequently, the HF-MAPs' contact with the fluids in the receiver compartment was limited and resulted in less swelling compared to the dermatomed skin setup. Samples obtained from skin, swollen HF-MAPs and ATR-containing reservoir residuals were quantified and analyzed. Fig. 7E represents the ATR quantity (mg) obtained from each compartment of Franz-cells at 4 and 24 h, respectively. The results show that, upon comparing both time points, there was no significant difference in the ATR amount recovered from each compartment ($p > 0.05$). Additionally, there was no significant difference in the total amount of ATR recovered from all compartments in both studies after 4 and 24 h (10.17 ± 0.16 mg and 10.13 ± 1.13 mg, respectively). This suggests that similar amounts of ATR were deposited in the skin at both time points, as shown in Fig. 7F. A comparison between the amount of ATR deposited in both full-thickness and dermatomed skin setups at 24 h is presented in Fig. 7G. Herein, it was revealed that significantly more ATR ($p < 0.0001$) was recovered from the receiver compartment of Franz cells and skin upon using dermatomed skin compared to the full-thickness skin. On the other hand, significantly more ATR was retrieved from the HF-MAPs when using full-thickness skin ($p = 0.0002$). This can be attributed to the higher thickness of the skin, which could have resulted in less hydration of the HF-MAPs compared to the dermatomed skin. This might have allowed for the reservoir to dissolve and diffuse into the MAPs but not into the skin and subsequent receiver compartment. It might have required more time or hydration to diffuse through the MAPs into the skin and the receiver compartment. Once all Franz-cells were disassembled, images were taken of the skin and HF-MAPs after 4 and 24 h, as shown in Fig. 7(H—I) and Fig. 7(J-K), respectively.

The SEM images taken following the lyophilization of skin and HF-MAPs (Fig. 8) clearly demonstrate the presence of ATR inside the HF-MAPs and the pores created within the skin. This showed that ATR was delivered into the skin through the micro conduits created using HF-MAPs and made a microdepot in the skin. This could predict the potential long-acting delivery of ATR in the subsequent *in vivo* studies.

3.4. In vivo delivery of ATR from Sprague Dawley rats

3.4.1. In vivo delivery of ATR

The *in vivo* study was conducted to determine the possibility of translating the developed HF-MAPs and RF-2 reservoir SD system from an *ex vivo* setup into an animal model. HF-MAPs were inserted into the backs of female *Sprague Dawley* rats using manual thumb pressure and were left in place for 24 h. The pharmacokinetic parameters of ATR, following a single dose application, were evaluated in this *in vivo* study over 14 days. The appropriate insertion of the HF-MAPs into the skin of the rats plays a vital role in ensuring effective drug delivery. Moreover, the adhesion of a transdermal system onto the skin is considered a crucial factor governing drug delivery and, subsequently, therapeutic outcomes of the system [80,81]. In the instance of insufficient adhesion, therapeutic failure may be inevitable due to improper dosing, especially if the patch is removed sooner than required [82]. During the sampling points within the first 6 h and just before HF-MAPs removal at 24 h, it was promising to notice that the HF-MAPs remained intact, secure in their places, and did not move or cause any discomfort to the rats, despite their high mobility. Visible holes created by the insertion of HF-MAPs were observed on the application site (Fig. 9A), but the skin had fully recovered within an hour following their removal. In minor cases, a few rats displayed mild erythema at the application site at 24 h, as seen in Fig. 9B. However, it was entirely resolved within a few hours following the removal of MAPs, and no signs of erythema were seen on the following day [22,83]. Upon removing HF-MAPs, it was promising to find that RF-2 reservoirs were entirely dissolved with no residuals spotted within the system (Fig. 9C). Once removed, HF-MAPs demonstrated extensive swelling. Nevertheless, they were removed completely intact from the rats' skin, leaving no polymer residues behind (Fig. 9 D—F). These findings match previously reported results [11,12,22,29] and confirm the versatility of the developed HF-MAPs in terms of functionality and safety. The biocompatibility of HF-MAPs has been widely addressed in previous reports. One study carried out by Al-kasasbeh et al. addressed the clinical impact of the repeated insertion of HF-MAPs into the skin of human volunteers [84]. The results showed that the multiple reinsertions and prolonged wear of HF-MAPs did not have an impact on skin barrier function or cause prolonged skin reactions. The concentrations of particular systemic biomarkers of inflammation (C-reactive protein (CRP); tumor necrosis factor-α (TNF-α)); infection (interleukin-1β (IL-1β)); allergy (immunoglobulin E (IgE)) and immunity (immunoglobulin G (IgG)) were all measured during the study period. Over the duration of the trial, no biomarker values above the typical, reported adult levels were detected, indicating that no systemic reactions were initiated in volunteers [84]. Another study published by Donnelly *et al,* in 2014, proves that HF-MAPs can still be removed completely intact from the skin following their swelling, without affecting the skin barrier function [22]. An additional study, published by Donnelly et al. in 2012, measures the biocompatibility of the hydrogel materials with cells in cultures, as well as 3D reconstructed epidermal models. An indirect test with two suspended cell lines, fibroblasts (Balb/3 T3) and keratinocytes (NRERT-1)24, and a 3D keratinocyte organotypic raft culture were used. The results showed no signs of significant reduction of cell viability in all three different tests, indicating the biocompatibility of the hydrogels [11].

The *in vivo* plasma profile of ATR from the rats of both cohorts is presented in Fig. 10A. An immediate increase in the plasma concentration of ATR following its oral administration can be observed. This is indicated by the elevated plasma concentration of ATR (C_{max} of 998.2 ±

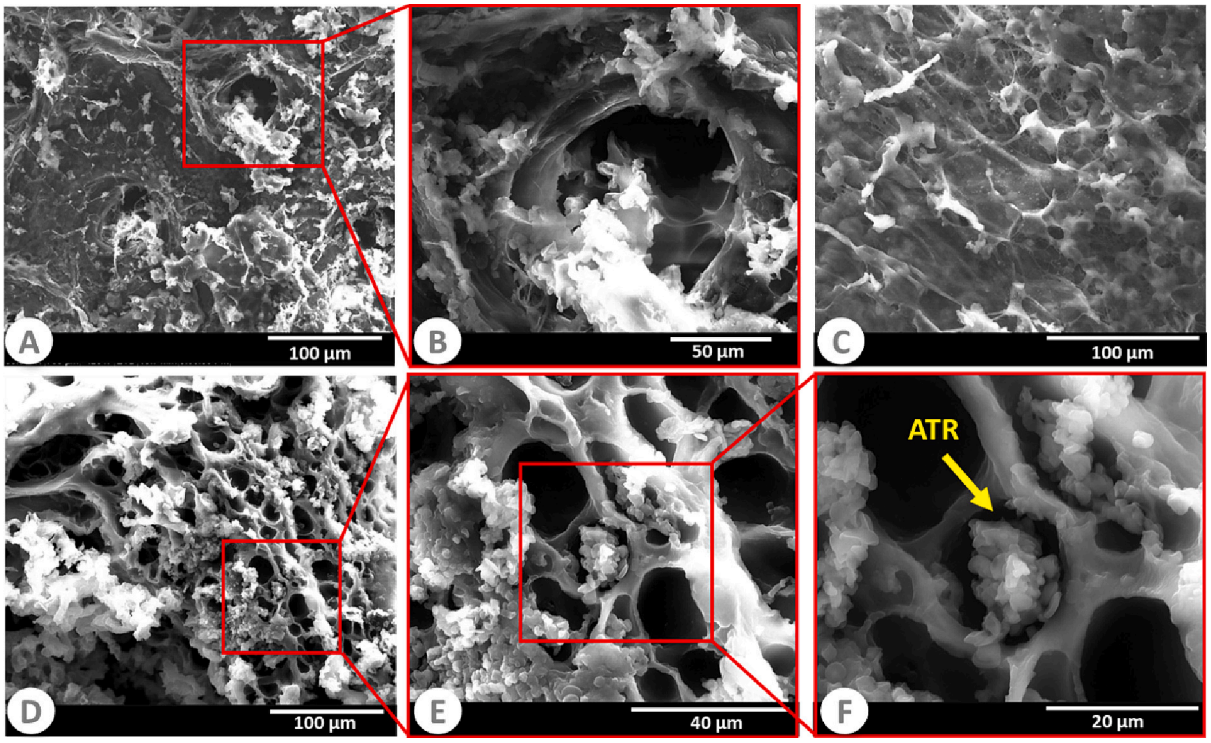

Fig. 8. SEM images of the lyophilized skin and HF-MAPs samples following an *ex vivo* study. (A) Shows the pores created in the upper surface of the porcine skin following the insertion of the HF-MAPs and the delivery of ATR from the PEG reservoir across them. (B) A zoom into one of the pores, where ATR (small particles) can be seen within the pores. (C) The lower side of the porcine skin, where ATR (small particles) can also be seen. (D) HF-MAPs image, showing the pores created as a result of the HF-MAPs swelling. ATR can be seen (small particles) all around the swollen hydrogel pores. (E) A zoom into some of the hydrogel pores showing ATR inside them. (F) A closer image to one of the pores, with ATR particles seen inside.

306.3 ng·mL^{-1}) at $t = 1$ h (T_{max} in this case). It started to decline sharply afterwards to reach a concentration of 24.3 ± 6.7 ng·mL^{-1} at 24 h before it completely collapsed below the limit of quantification of the method (20 ng·mL^{-1}) after that time point. The plasma concentration of the HF-MAPs cohort rats was shown to possess a delayed initial response compared to the control group. This was expected and can be attributed to the time required for the HF-MAPs to imbibe the interstitial fluid and swell. Upon their swelling, HF-MAPs were able to dissolve the ATR reservoir laid on their surfaces, allowing for the diffusion of ATR across their swollen matrix and into the dermal layers of the skin, where it was taken up by the dermal microcirculation. Consequently, at $t = 2$ h (T_{max}), plasma levels of ATR started to increase significantly and reached a C_{max} of 275.2 ± 88.9 ng·mL^{-1}. Afterwards, they began to gradually decrease, reaching a concentration of 93 ± 55.9 ng·mL^{-1} at 24 h. The ATR plasma levels on the second day were highly similar to those at the 24 h time point. From the third day onwards, ATR plasma levels were relatively consistent, with a concentration starting from 46.9 ± 17.9 ng·mL^{-1} on the third day and reaching 36.6 ± 24.8 ng·mL^{-1} on the last day of the study. Sustained delivery of ATR from HF-MAPs was maintained throughout the study period of 14 days. This is considered a novel aspect of this work, as it is the first time that the feasibility of long-acting delivery of a hydrophobic compound using HF-MAPs combined with PEG-based SD reservoirs has been reported. A therapeutically-relevant concentration of ATR was observed in the cohorts receiving HF-MAPs within the first hour [85,86] and was maintained thereafter throughout the entire study period.

In 2017, Mahmoud *et al* reported the use of nanovesicular system encapsulating ATR for its transdermal drug delivery. Their optimized vesicular systems were created by combining phosphatidylcholine and Gelucire 44/14 in a 15:1 M ratio and 10 mg of ATR. In their *in vivo* study, rats received this optimized nanotransfersomal gel formulation. Their abdominal area was shaved, and 1 g of the gel was applied over a surface area of 20 cm^2. The results has shown a successful transdermal delivery of ATR for only 72 h [87]. Another study conducted by El-Say *et al* in 2021, investigated the use of an oleic acid–reinforced PEGylated polymethacrylate transdermal film as an alternative delivery system for ATR. Using the Quality by Design (QbD) technique, they optimized the influence of varied quantities of Eudragit RLPO, PEG 400, and oleic acid on the desired product profile. The studied the *in vivo* transdermal delivery of their optimized film formulation using rats. Each film (6.74 cm^2) contained approximately 200 mg of ATR. They managed to achieve transdermal delivery of ATR for 72 h [88]. On the other hand, this article reports, for the first time, the long-acting delivery of ATR over 14 days. Furthermore, the patch size used in this work was 2 cm^2, which is 10 times smaller than the area Mahmoud *et al* required to deliver ATR from their gels over 72 h [87] and is approximately the third of the area of El-Say *et al* films [88]. Moreover, the reproducibility of applying the same dose of the cream every time may also be unreliable, especially when compared to the known drug-loading of each HF-MAP. This demonstrates the superiority of HF-MAPs combined with the SD PEG-based reservoirs in terms of patch area, dosing, and performance in the transdermal long-acting delivery of ATR, as a model hydrophobic agent, over prolonged periods of time.

The reservoir formulation, where ATR was incorporated into the PEG matrix using an SD technique, had played a vital role in those findings. Since PEG is a water-soluble polymer, it will have been readily taken up by the dermal microcirculation once it reached the dermis. The initial surge in the C_{max} of ATR at $t = 2$ h could be attributed to the amount of ATR dissolved within the PEG and was able to be immediately absorbed into the bloodstream. Due to the hydrophobic nature of ATR, the remaining amount delivered would have formed a microdepot within the skin layers, from which it was slowly dissolved and released over the study period. Consequently, therapeutically-relevant concentrations of ATR were detected throughout the study. This microdepot, formed

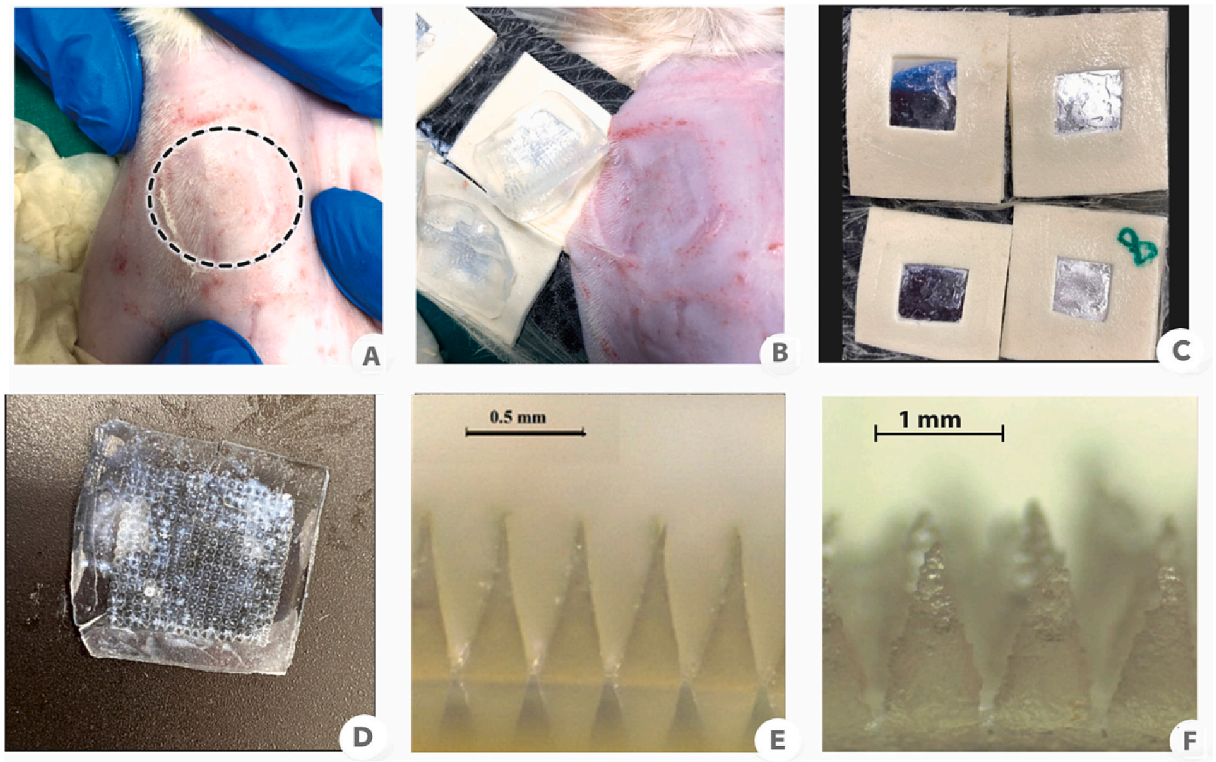

Fig. 9. Digital and microscopic images taken 24 h after the application of HF-MAPs to the rats and immediately upon their removal. (A) The site of application of a HF-MAP. (B) The removal of the swollen HF-MAPs from the rats' backs completely intact without leaving any polymer behind. (C) The backing adhesive layer, where reservoirs were inserted prior to their application, attached to Tegaderm™ adhesive tape and kinesiology surgical tape from the rodents. Also shows the complete disappearance of the RF-2 drug reservoir, which indicates its complete dissolution and the delivery of its contents to the animal. (D) A swollen HF-MAP upon its removal from the skin and backing layer. (E) A digital microscopic image of the a HF-MAP prior to its insertion into the rat skin (scale bar = 0.5 mm). (F) A digital microscopic image of the swollen HF-MAP following its removal from rat skin during the *in vivo* study (scale bar = 1 mm).

within the skin, was the key player in the long-acting delivery of ATR using this unique system. To the best of the authors' knowledge, it has never been proven before that ATR can be transdermally delivered as a microdepot, from which a therapeutic dose can be released in a controlled manner over 2 weeks. Furthermore, the long-acting delivery of ATR using HF-MAPs has never been addressed previously. Additionally, this is the first report of the successful use of PEG-based SD reservoirs in combination with HF-MAPs for the long-acting delivery of a hydrophobic compound. Moreover, this is the first study to describe the usage of HF-MAPs to deliver hydrophobic drugs in therapeutically-relevant doses for treatment purposes over a prolonged period of time. Therefore, all these points are considered novel aspects of the present work.

3.4.2. Pharmacokinetic analysis

The use of the HF-MAPs formulation could enhance the overall pharmacokinetics profile of ATR in plasma compared to the oral group, as shown in Table 4. ATR promptly reaches the systemic circulation following oral administration but is then swiftly eliminated. This was to be expected and explains the short-term efficacy and the frequent administration of ATR delivered *via* this route [90]. Conversely, HF-MAPs displayed a slower T_{max} than the oral control and offered a sustained release of ATR over 2 weeks. Moreover, the prolonged release of ATR achieved using HF-MAPs resulted in approximately ten folds higher systemic exposure levels than the oral control. Significantly ($p < 0.05$) higher $AUC_{0–14}$ values of 678.35 ± 351.63 ng·mL^{-1}·day were obtained from HF-MAPs compared to values of the oral group (197.05 ± 106.6 ng·mL^{-1}·day). The $AUC_{0\text{-inf\_obs}}$ obtained from the HF-MAPs group was 2336.58 ± 2146.98 ng·mL^{-1}·day, which was higher than that of the control group (222.97 ± 116.45 ng·mL^{-1}·day). Furthermore, HF-MAPs attained MRT values of 34.98 ± 33.31 days, which were significantly ($p < 0.05$) higher than those of the control group (0.61 ± 0.35 days). Fig. 10(B—D) summarizes these findings. Therapeutically relevant concentrations (> 10 ng·mL^{-1}) were quantified throughout the study [85,89], proving the versatility of HF-MAPs technology in combination with the PEG-based SD reservoirs for the first time in the long-acting delivery of ATR.

3.4.3. Estimation of actual patch size for humans

Upon the cautious extrapolation of the information obtained from this study, an approximate patch size was estimated. ATR is given in an oral dose ranging from 10 to 80 mg·day^{-1}, where the oral bioavailability is approximately 14% [78,89,91]. Therefore, to provide a dose equivalent to 40 mg·day^{-1} in humans, roughly 5.6 mg of ATR needs to be delivered transdermally using HF-MAPs. Given that the amount of ATR delivered from 4 HF-MAPs possessing a total area of 2 cm^2 was approximately 4.82 mg (estimated based on the *in vivo* $AUC_{0\text{-t}}$ values and ATR dose), a patch size of 2.3 cm^2 could potentially deliver therapeutically relevant concentration, equivalent to an oral dose of 40 mg·day^{-1}. Therefore, a patch size of 32.5 cm^2 would be sufficient to provide therapeutically-relevant plasma concentration of ATR over 2 weeks from a single HF-MAP application for only 24 h. This area is considered within the acceptable range of commercially-available conventional transdermal patches, with the commonly used fentanyl-loaded transdermal patch possessing an area of approximately 42 cm^2 [92].

The potential of the long-acting delivery of ATR using HF-MAPs can positively impact the quality of life for patients. It can improve their compliance with their treatment regimens by reducing dosing frequencies and thus enhancing therapeutic outcomes [93,94]. Furthermore, HF-MAPs were proven to be safe to use, with a self-disabling design aiding in decreasing the likelihood of mistaken reinsertion [22]. Therefore, HF-MAPs technology combined with PEG-based ATR SD

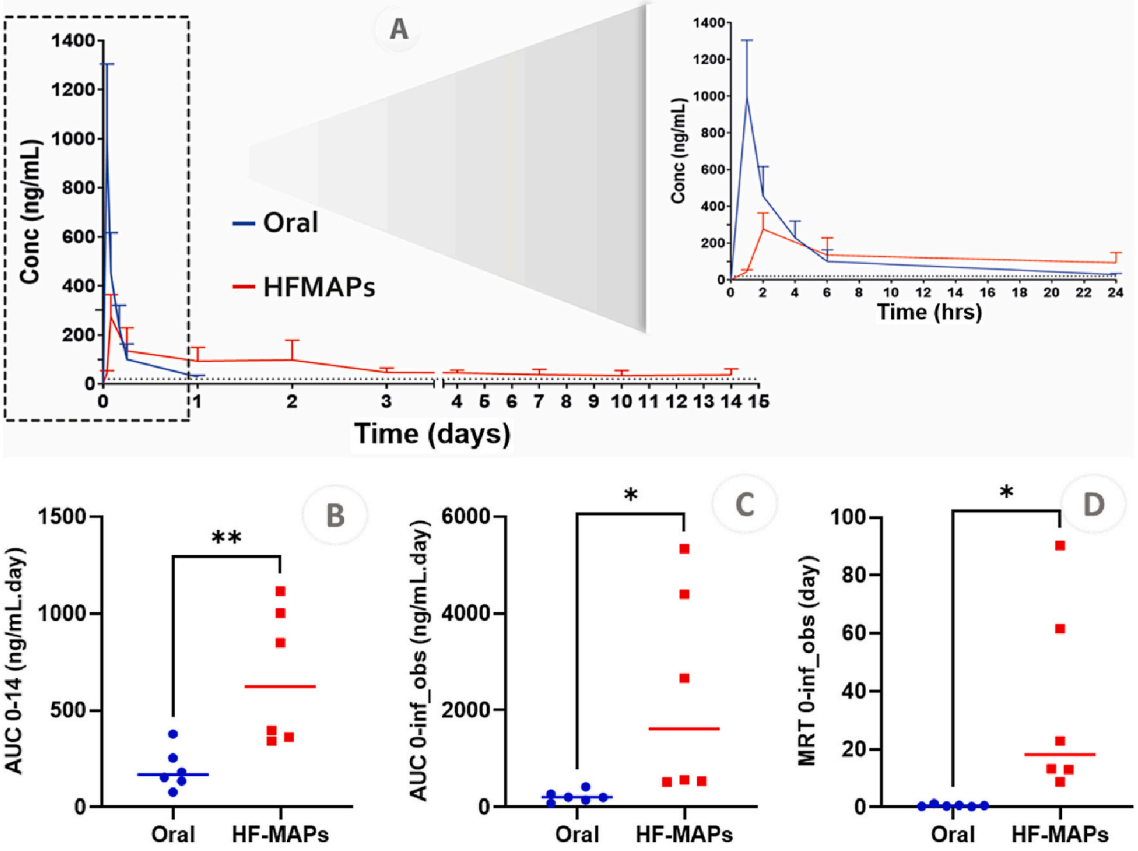

Fig. 10. (A) ATR plasma profiles of the rats from the oral and HF-MAPs cohorts following the *in vivo* study for 14 days. (Means + S.Ds., $n = 6$ at 1, 2, 4 and 6 h, $n = 12$ at the remaining time points). The black dashed line represents the LOQ of the analytical method (20 ng·mL^{-1}). It also represents the therapeutic dose of ATR in rats over 6 h following the oral administration of ATR [89]. Statistical analysis and representation of (B) $AUC_{0–14}$, (C) $AUC_{0\text{-inf\_obs}}$, (D) and $MRT_{0\text{-inf\_obs}}$ in rats from both cohorts. Each point on the graph represents one rat (total n = 12). (**$p = 0.0093$, *$p < 0.0368$).

Table 4
In vivo plasma pharmacokinetic parameters of ATR after oral and HF-MAPs administration to *Sprague Dawley* rats. (Means ± S.Ds., n = 6 for each group).

Parameter	Unit	Control (oral)	HF-MAPs
T_{max}	hour	1	2
C_{max}	ng·mL^{-1}	998.2 ± 306.3	275.2 ± 88.9
$AUC_{0\text{-t}}$	ng·mL^{-1}·day	197.05 ± 106.6	678.35 ± 351.63
$AUC_{0\text{-inf\_obs}}$	ng·mL^{-1}·day	222.97 ± 116.45	2336.58 ± 2146.98
$MRT_{0\text{-inf\_obs}}$	day	0.61 ± 0.35	34.98 ± 33.31

reservoirs possesses the potential to enhance patient outcomes by providing a pain-free delivery method that maximizes the therapeutic effect over prolonged periods.

4. Conclusion

This work described, for the first time, the versality of HF-MAPs in the long-acting delivery of ATR over two weeks. The system was comprised of HF-MAPs in combination with PEG-based ATR SD reservoirs, and could successfully deposit ATR in the rat model within a 24 h application time and provided therapeutically-relevant concentrations over 14 days. The solubilization of ATR in the PEG-based SD reservoirs provided a promising means to facilitate the transdermal delivery of this hydrophobic agent across the aqueous conduits of the HF-MAPs and into the skin. This novel technology offers a potential platform with broad applicability in terms of depot-delivery of many hydrophobic drugs for long-acting release and absorption. This system can overcome various obstacles associated with the available parenteral and implantable long-acting delivery devices in terms of being a self-applicable painless drug delivery method. These findings suggest that HF-MAPs technology can be used to expand the range of drugs delivered transdermally to include hydrophobic agents. SD is a straightforward, well-reported solubility enhancement method that can be easily scaled up to an industrial manufacturing setup, hence, increasing the chances of commercialization of this novel system. Moving forward, there are various priorities that must be addressed in terms of large-scale manufacturing, commercialization, and eventually, patient usage of a MAP product. Future studies could include a pharmacological animal study in which the correlation between drug bioavailability and treatment efficacy is further investigated prior to performing a clinical trial to evaluate the safety and pharmacokinetics in humans. Future work may also involve the regulatory bodies' criteria for MAP products, as well as whether manufacturing under aseptic conditions would be necessary or end-product sterilization is rather required. These factors will be critical in determining whether the product can be commercialized on a wide scale while still being cost-effective, without neglecting the ultimate aim of enhancing patients' compliance and improving the quality of their lives.

CRediT authorship contribution statement

Yara A. Naser: Investigation, Methodology, Formal analysis, Data curation, Conceptualization, Writing – original draft, Writing – review & editing. **Ismaiel A. Tekko:** Investigation, Methodology, Formal analysis, Data curation, Writing – review & editing. **Lalitkumar K. Vora:** Investigation, Formal analysis, Data curation, Writing – review & editing. **Ke Peng:** Investigation, Formal analysis. **Qonita K. Anjani:** Investigation, Formal analysis. **Brett Greer:** Formal analysis, Resources. **Christopher Elliott:** Resources. **Helen O. McCarthy's:** Resources.

Ryan F. Donnelly: Conceptualization, Supervision, Methodology, Formal analysis, Resources, Funding acquisition, Writing – review & editing.

Declaration of Competing Interest

None.

Data availability

Data will be made available on request.

Acknowledgements

This work was based on a part of Yara A. Naser's PhD thesis. The authors would like to thank Mr. Achmad Himawan for his kind support during the write up of this manuscript, and Dr. Ana Carolina Andrade Vitor for her help in optimizing the Figures.

Appendix A. Supplementary data

Supplementary data to this article can be found online at https://doi.org/10.1016/j.jconrel.2023.03.003.

References

[1] E. Larrañeta, T.R.R. Singh, R.F. Donnelly, Overview of the clinical current needs and potential applications for long-acting and implantable delivery systems, in: Long-Acting Drug Delivery Systems, Elsevier, 2022, pp. 1–16.
[2] S.I. Shen, B.R. Jasti, X. Li, Design of controlled-release drug delivery systems, in: M. Kutz (Ed.), Standard Handbook of Biomedical Engineering & Design, 1 edition, McGraw-Hill Education, New York, 2003, pp. 161–179.
[3] S.I. Jethara, M.R. Patel, A.D. Patel, Sustained release drug delivery systems: a patent overview, Aperito J. Drug Desig. Pharmacol. 1 (2014) 104.
[4] V. Vijayakumar, K.G. Subramanian, Drug carriers, polymers as: synthesis, characterization, and *in vitro* evaluation, in: Encyclopedia of Biomedical Polymers and Polymeric Biomaterials, 2016, pp. 1–28.
[5] Y. Shi, L.C. Li, Current advances in sustained-release systems for parenteral drug delivery, Expert Opin. Drug Deliv. 2 (2005) 1039–1058.
[6] S.A. Stewart, J. Dominguez-Robles, R.F. Donnelly, E. Larraneta, Implantable polymeric drug delivery devices: classification, manufacture, materials, and clinical applications, Polymers (Basel) 10 (2018) 1379.
[7] J.H. Jung, S.G. Jin, Microneedle for transdermal drug delivery: current trends and fabrication, J. Pharm. Investig. 51 (2021) 503–517.
[8] D. Ramadon, M.T. McCrudden, A.J. Courtenay, R.F. Donnelly, Enhancement strategies for transdermal drug delivery systems: current trends and applications, Drug Deliv. Transl. Res. 12 (2022) 758–791.
[9] R. Kharat, R.S. Bathe, A comprehensive review on: transdermal drug delivery systems, Intern. J. Biomed. Adv. Res. 7 (2016) 147–159.
[10] J.J. Escobar-Chávez, R. Díaz-Torres, I.M. Rodríguez-Cruz, C.L. Domínguez-Delgado, R.S. Morales, E. Ángeles-Anguiano, L.M. Melgoza-Contreras, Nanocarriers for transdermal drug delivery, Res. Reports Transd. Drug Deliv. 1 (2012) 3.
[11] R.F. Donnelly, T.R.R. Singh, M.J. Garland, K. Migalska, R. Majithiya, M.T. C. McCrudden, P.L. Kole, T.M. Mahmood, H.O. McCarthy, A.D. Woolfson, Hydrogel-forming microneedle arrays for enhanced transdermal drug delivery, Adv. Funct. Mater. 22 (2012) 4879–4890.
[12] R.F. Donnelly, M.T.C. McCrudden, A.Z. Alkilani, E. Larraneta, E. McAlister, A. J. Courtenay, M.C. Kearney, T.R.R. Singh, H.O. McCarthy, V.L. Kett, et al., Hydrogel-forming microneedles prepared from "super swelling" polymers combined with lyophilised wafers for transdermal drug delivery, PLoS One 9 (2014), e111547.
[13] E. Larrañeta, R.E.M. Lutton, A.D. Woolfson, R.F. Donnelly, Microneedle arrays as transdermal and intradermal drug delivery systems: materials science, manufacture and commercial development, Mater. Sci. Eng. R. Rep. 104 (2016) 1–32.
[14] R.F. Donnelly, T.R.R. Singh, A.Z. Alkilani, M.T.C. McCrudden, S. O'Neill, C. O'Mahony, K. Armstrong, N. McLoone, P. Kole, A.D. Woolfson, Hydrogel-forming microneedle arrays exhibit antimicrobial properties: potential for enhanced patient safety, Int. J. Pharm. 451 (2013) 76–91.
[15] M.T.C. McCrudden, A.Z. Alkilani, C.M. McCrudden, E. McAlister, H.O. McCarthy, A.D. Woolfson, R.F. Donnelly, Design and physicochemical characterisation of novel dissolving polymeric microneedle arrays for transdermal delivery of high dose, low molecular weight drugs, J. Control. Release 180 (2014) 71–80.
[16] S. Khan, M.U. Minhas, I.A. Tekko, R.F. Donnelly, R.R.S. Thakur, Evaluation of microneedles-assisted in situ depot forming poloxamer gels for sustained transdermal drug delivery, Drug Deliv. Transl. Res. 9 (2019) 764–782.
[17] R.F. Donnelly, R. Majithiya, T.R.R. Singh, D.I.J. Morrow, M.J. Garland, Y.K. Demir, K. Migalska, E. Ryan, D. Gillen, C.J. Scott, A.D. Woolfson, Design, optimization and characterisation of polymeric microneedle arrays prepared by a novel laser-based micromoulding technique, Pharm. Res. 28 (2011) 41–57.
[18] P.R. Yadav, M.I. Nasiri, L.K. Vora, E. Larrañeta, R.F. Donnelly, S.K. Pattanayek, D. B. Das, Super-swelling hydrogel-forming microneedle based transdermal drug delivery: mathematical modelling, simulation and experimental validation, Int. J. Pharm. 121835 (2022).
[19] I.A. Tekko, G. Chen, J. Domínguez-Robles, R.R.S. Thakur, I.M.N. Hamdan, L. Vora, E. Larrañeta, J.C. McElnay, H.O. McCarthy, M. Rooney, R.F. Donnelly, Development and characterisation of novel poly (vinyl alcohol)/poly (vinyl pyrrolidone)-based hydrogel-forming microneedle arrays for enhanced and sustained transdermal delivery of methotrexate, Int. J. Pharm. 586 (2020), 119580.
[20] R.F. Donnelly, M.J. Garland, D.I. Morrow, K. Migalska, T.R.R. Singh, R. Majithiya, A.D. Woolfson, Optical coherence tomography is a valuable tool in the study of the effects of microneedle geometry on skin penetration characteristics and in-skin dissolution, J. Control. Release 147 (2010) 333–341.
[21] R.F. Donnelly, K. Moffatt, A.Z. Alkilani, E.M. Vicente-Perez, J. Barry, M.T. C. McCrudden, A.D. Woolfson, Hydrogel-forming microneedle arrays can be effectively inserted in skin by self-application: a pilot study centred on pharmacist intervention and a patient information leaflet, Pharm. Res. 31 (2014) 1989–1999.
[22] R.F. Donnelly, K. Mooney, M.T.C. McCrudden, E.M. Vicente-Perez, L. Belaid, P. Gonzalez-Vazquez, J.C. McElnay, A.D. Woolfson, Hydrogel-forming microneedles increase in volume during swelling in skin, but skin barrier function recovery is unaffected, J. Pharm. Sci. 103 (2014) 1478–1486.
[23] H.L. Quinn, R.F. Donnelly, Transdermal applications of hydrogels, in: T.R.R. S, G. Laverty (Eds.), Hydrogels: Design, Synthesis and Application in Drug Delivery and Regenerative Medicine, 1 edition vol. 1, CRC Press, Donnelly RF, 2018, pp. 250–264.
[24] M. Bahram, N. Mohseni, M. Moghtader, An introduction to hydrogels and some recent applications, in: S.B. Majee (Ed.), Emerging Concepts in Analysis and Applications of Hydrogels, IntechOpen, 2016, pp. 9–38.
[25] N.A. Peppas, Hydrogels in pharmaceutical formulations, Eur. J. Pharm. Biopharm. 50 (2000) 27–46.
[26] J. Li, D.J. Mooney, Designing hydrogels for controlled drug delivery, Nat. Rev. Mater. 1 (2016) 1–17.
[27] R.F. Donnelly, D.I. Morrow, M.T.C. McCrudden, A.Z. Alkilani, E.M. Vicente-Perez, C. O'Mahony, P. Gonzalez-Vazquez, P.A. McCarron, A.D. Woolfson, Hydrogel-forming and dissolving microneedles for enhanced delivery of photosensitizers and precursors, J. Photochem. Photobiol. 90 (2014) 641–647.
[28] M.I. Nasiri, L.K. Vora, J.A. Ershaid, K. Peng, I.A. Tekko, R.F. Donnelly, Nanoemulsion-based dissolving microneedle arrays for enhanced intradermal and transdermal delivery, Drug Deliv. Transl. Res. 12 (2022) 881–896.
[29] E.M. Migdadi, A.J. Courtenay, I.A. Tekko, M.T.C. McCrudden, M.C. Kearney, E. McAlister, H.O. McCarthy, R.F. Donnelly, Hydrogel-forming microneedles enhance transdermal delivery of metformin hydrochloride, J. Control. Release 285 (2018) 142–151.
[30] A.J. Courtenay, E. McAlister, M.T.C. McCrudden, L. Vora, L. Steiner, G. Levin, E.S. N. Levy-Nissenbaum, M.C. Kearney, McCarthy HO, R.F. Donnelly, Hydrogel-forming microneedle arrays as a therapeutic option for transdermal esketamine delivery, J. Control. Release 322 (2020) 177–186.
[31] E. McAlister, B. Dutton, L.K. Vora, L. Zhao, A. Ripolin, D.S.Z.B.P.H. Zahari, H. L. Quinn, I.A. Tekko, A.J. Courtenay, S.A. Kelly, et al., Directly compressed tablets: a novel drug-containing reservoir combined with hydrogel-forming microneedle arrays for transdermal drug delivery, Adv. Healthcare Mater. 10 (2021) 2001256.
[32] A.J. Courtenay, M.T.C. McCrudden, K.J. McAvoy, H.O. McCarthy, R.F. Donnelly, Microneedle-mediated transdermal delivery of bevacizumab, Mol. Pharm. 15 (2018) 3545–3556.
[33] A. Kumar, S.K. Sahoo, K. Padhee, P.S. Kochar, A. Sathapathy, N. Pathak, Review on solubility enhancement techniques for hydrophobic drugs, Pharm. Glob. 3 (2011) 001–007.
[34] A. Fahr, X. Liu, Drug delivery strategies for poorly water-soluble drugs, Expert Opin. Drug Deliv. 4 (4) (2007) 403–416.
[35] S. Kalepu, V. Nekkanti, Insoluble drug delivery strategies: review of recent advances and business prospects, Acta Pharm. Sin. B 5 (2015) 442–453.
[36] M. Li, L.K. Vora, K. Peng, R.F. Donnelly, Trilayer microneedle array assisted transdermal and intradermal delivery of dexamethasone, Int. J. Pharm. 612 (2022), 121295.
[37] K. Sekiguchi, N. Obi, Studies on absorption of eutectic mixture. I. a comparison of the behavior of eutectic mixture of sulfathiazole and that of ordinary sulfathiazole in man, Chem. Pharm. Bull. 9 (1961) 866–872.
[38] K. Sekiguchi, N. Obi, Y. Ueda, Studies on absorption of eutectic mixture. II. Absorption of fused conglomerates of chloramphenicol and urea in rabbits, Chem. Pharm. Bull. 12 (1964) 134–144.
[39] P. Tran, Y.C. Pyo, D.H. Kim, S.E. Lee, J.K. Kim, J.S. Park, Overview of the manufacturing methods of solid dispersion technology for improving the solubility of poorly water-soluble drugs and application to anticancer drugs, Pharmaceutics 11 (2019) 132.
[40] A. Haser, T. Cao, J. Lubach, T. Listro, L. Acquarulo, F. Zhang, Melt extrusion vs. spray drying: the effect of processing methods on crystalline content of naproxen-povidone formulations, Eur. J. Pharm. Sci. 102 (2017) 115–125.
[41] R. Ghanavati, A. Taheri, A. Homayouni, Anomalous dissolution behavior of celecoxib in PVP/Isomalt solid dispersions prepared using spray drier, Mater. Sci. Eng. C 72 (2017) 501–511.
[42] J.O. Eloy, J.M. Marchetti, Solid dispersions containing ursolic acid in Poloxamer 407 and PEG 6000: a comparative study of fusion and solvent methods, Powder Technol. 253 (2014) 98–106.

[43] D.P. Otto, A. Otto, M.M. de Villiers, Experimental and mesoscale computational dynamics studies of the relationship between solubility and release of quercetin from PEG solid dispersions, Int. J. Pharm. 456 (2013) 282–292.
[44] J.N. Reginald-Opara, A. Attama, K. Ofokansi, C. Umeyor, F. Kenechukwu, Molecular interaction between glimepiride and Soluplus®-PEG 4000 hybrid based solid dispersions: characterisation and anti-diabetic studies, Int. J. Pharm. 496 (2015) 741–750.
[45] J. Huang, R.J. Wigent, C.M. Bentzley, J.B. Schwartz, Nifedipine solid dispersion in microparticles of ammonio methacrylate copolymer and ethylcellulose binary blend for controlled drug delivery: effect of drug loading on release kinetics, Int. J. Pharm. 319 (2006) 44–54.
[46] A. Ceballos, M. Cirri, F. Maestrelli, G. Corti, P. Mura, Influence of formulation and process variables on *in vitro* release of theophylline from directly-compressed eudragit matrix tablets, Il Farmaco 60 (2005) 913–918.
[47] S. Afifi, Solid dispersion approach improving dissolution rate of stiripentol: a novel antiepileptic drug, Iran. J. Pharm. Res. 14 (2015) 1001.
[48] S. Alshehri, S.S. Imam, M.A. Altamimi, A. Hussain, F. Shakeel, E. Elzayat, K. Mohsin, M. Ibrahim, F. Alanazi, Enhanced dissolution of luteolin by solid dispersion prepared by different methods: physicochemical characterization and antioxidant activity, ACS Omega 5 (2020) 6461–6471.
[49] L.A. Nikghalb, G. Singh, G. Singh, K.F. Kahkeshan, Solid dispersion: methods and polymers to increase the solubility of poorly soluble drugs, J. Appl. Pharm. Sci. 2 (2012) 170–175.
[50] M. Demasi, Statin wars: have we been misled about the evidence? A narrative review, Br. J. Sports Med. 52 (2018) 905–909.
[51] M.S. Rodde, G.T. Divase, T.B. Devkar, A.R. Tekade, Solubility and bioavailability enhancement of poorly aqueous soluble atorvastatin: in vitro, ex vivo, and in vivo studies, Biomed. Res. Int. 2014 (2014), 463895.
[52] R. Löbenberg, G.L. Amidon, Modern bioavailability, bioequivalence and biopharmaceutics classification system. New scientific approaches to international regulatory standards, Eur. J. Pharm. Biopharm. 50 (2000) 3–12.
[53] E. Larraneta, J. Moore, E.M. Vicente-Perez, P. Gonzalez-Vazquez, R. Lutton, A. D. Woolfson, R.F. Donnelly, A proposed model membrane and test method for microneedle insertion studies, Int. J. Pharm. 472 (2014) 65–73.
[54] L.K. Vora, R.F. Donnelly, E. Larrañeta, P. González-Vázquez, R.R.S. Thakur, P. R. Vavia, Novel bilayer dissolving microneedle arrays with concentrated PLGA nano-microparticles for targeted intradermal delivery: proof of concept, J. Control. Release 265 (2017) 93–101.
[55] H. Jiang, H. Zheng, Efficacy and adverse reaction to different doses of atorvastatin in the treatment of type II diabetes mellitus, Biosci. Rep. 39 (2019) 1–10.
[56] A.H. Sabri, Y. Kim, M. Marlow, D.J. Scurr, J. Segal, A.K. Banga, L. Kagan, J.B. Lee, Intradermal and transdermal drug delivery using microneedles – fabrication, performance evaluation and application to lymphatic delivery, Adv. Drug Deliv. Rev. 153 (2020) 195–215.
[57] M.T.C. McCrudden, E. Larrañeta, A. Clark, C. Jarrahian, A. Rein-Weston, S. Lachau-Durand, N. Niemeijer, P. Williams, C. Haeck, H.O. McCarthy, et al., Design, formulation and evaluation of novel dissolving microarray patches containing a long-acting rilpivirine nanosuspension, J. Control. Release 292 (2018) 119–129.
[58] K. Peng, L.K. Vora, J. Domínguez-Robles, Y.A. Naser, M. Li, E. Larrañeta, R. F. Donnelly, Hydrogel-forming microneedles for rapid and efficient skin deposition of controlled release tip-implants, Mater. Sci. Eng. C 127 (2021), 112226.
[59] G.K. Menon, New insights into skin structure: scratching the surface, Adv. Drug Deliv. Rev. 54 (Suppl. 1) (2002) S3–17.
[60] S. Nafisi, H.I. Maibach, Chapter 3 - skin penetration of nanoparticles, in: R. Shegokar, E.B. Souto (Eds.), Emerging Nanotechnologies in Immunology, Elsevier, Boston, 2018, pp. 47–88.
[61] J.E. Lai-Cheong, J.A. McGrath, Structure and function of skin, hair and nails, Medicine 41 (2013) 317–320.
[62] X. Lin, F. Bao, C. Tu, Z. Yin, X. Gao, J. Lin, Dynamics of bubble formation in highly viscous liquid in co-flowing microfluidic device, Microfluid. Nanofluid. 23 (2019) 1–9.
[63] N. Kashyap, N. Kumar, M. Kumar, Hydrogels for pharmaceutical and biomedical applications, Crit. Rev. Ther. Drug Carrier Syst. 22 (2005) 107–149.
[64] S. Khan, A. Ullah, K. Ullah, N.U. Rehman, Insight into hydrogels, Desig. Monomers Poly. 19 (2016) 456–478.
[65] Q.K. Anjani, A.D. Permana, Á. Cárcamo-Martínez, J. Domínguez-Robles, I. A. Tekko, E. Larrañeta, L.K. Vora, D. Ramadon, R.F. Donnelly, Versatility of hydrogel-forming microneedles in *in vitro* transdermal delivery of tuberculosis drugs, Eur. J. Pharm. Biopharm. 158 (2021) 294–312.
[66] M.C. Kearney, P.E. McKenna, H.L. Quinn, A.J. Courtenay, E. Larraneta, R. F. Donnelly, Design and development of liquid drug reservoirs for microneedle delivery of poorly soluble drug molecules, Pharmaceutics 11 (2019) 605.
[67] S.H. Gehrke, J.P. Fisher, M. Palasis, M.E. Lund, Factors determining hydrogel permeability, Ann. N. Y. Acad. Sci. 831 (1997) 179–184.
[68] K.T. Savjani, A.K. Gajjar, J.K. Savjani, Drug solubility: importance and enhancement techniques, Intern. Scholarly Res. Notices 2012 (2012), 195727.
[69] A. Choudhary, A.C. Rana, G. Aggarwal, V. Kumar, F. Zakir, Development and characterization of an atorvastatin solid dispersion formulation using skimmed milk for improved oral bioavailability, Acta Pharm. Sin. B 2 (2012) 421–428.
[70] B.B. Eedara, M. Kankane, R. Jukanti, V.K. Nagabandi, S. Bandari, Enhanced solubility and permeability of exemestane solid dispersion powders for improved oral delivery, J. Pharm. Investig. 43 (2013) 229–242.
[71] G.V. Betageri, K.R. Makarla, Enhancement of dissolution of glyburide by solid dispersion and lyophilization techniques, Int. J. Pharm. 126 (1995) 155–160.
[72] A.M. Vargason, A.C. Anselmo, S. Mitragotri, The evolution of commercial drug delivery technologies, Nat. Biomed. Eng. 5 (2021) 951–967.
[73] R.J. Sengwa, K. Kaur, R. Chaudhary, Dielectric properties of low molecular weight poly (ethylene glycol)s, Polym. Int. 49 (2000) 599–608.
[74] J. Wu, C. Zhao, W. Lin, R. Hu, Q. Wang, H. Chen, L. Li, S. Chen, J. Zheng, Binding characteristics between polyethylene glycol (PEG) and proteins in aqueous solution, J. Mater. Chem. B 2 (2014) 2983–2992.
[75] E.P. da Silva, M.A.V. Pereira, I.P. de Barros Lima, N.G.P.B. Lima, E.G. Barbosa, C.F. S. Aragão, A.P.B. Gomes, Compatibility study between atorvastatin and excipients using DSC and FTIR, J. Therm. Anal. Calorim. 123 (2016) 933–939.
[76] PubChem compound summary for CID 60823, atorvastatin. https://pubchem.ncbi.nlm.nih.gov/compound/Atorvastatin.
[77] Y. Özkan, N. Doğanay, N. Dikmen, A. Işımer, Enhanced release of solid dispersions of etodolac in polyethylene glycol, Il Farmaco 55 (2000) 433–438.
[78] K.R. Bobe, C.R. Subrahmanya, S. Suresh, D.T. Gaikwad, M.D. Patil, T.S. Khade, B. B. Gavitre, V.S. Kulkarni, U.T. Gaikwad, Formulation and evaluation of solid dispersion of atorvastatin with various carriers, Intern. J. Compreh. Pharm. 2 (2011) 1–6.
[79] F.I. Kanaze, E. Kokkalou, I. Niopas, M. Georgarakis, A. Stergiou, D. Bikiaris, Dissolution enhancement of flavonoids by solid dispersion in PVP and PEG matrixes: a comparative study, J. Appl. Polym. Sci. 102 (2006) 460–471.
[80] S. Banerjee, P. Chattopadhyay, A. Ghosh, P. Datta, V. Veer, Aspect of adhesives in transdermal drug delivery systems, Int. J. Adhes. Adhes. 50 (2014) 70–84.
[81] S. Venkatraman, R. Gale, Skin adhesives and skin adhesion: 1. Transdermal drug delivery systems, Biomaterials 19 (1998) 1119–1136.
[82] A. Wokovich, S. Prodduturi, W. Doub, A. Hussain, L. Buhse, Transdermal drug delivery system (TDDS) adhesion as a critical safety, efficacy and quality attribute, Eur. J. Pharm. Biopharm. 64 (2006) 1–8.
[83] A. Ripolin, J. Quinn, E. Larraneta, E.M. Vicente-Perez, J. Barry, R.F. Donnelly, Successful application of large microneedle patches by human volunteers, Int. J. Pharm. 521 (2017) 92–101.
[84] R. Al-Kasasbeh, A.J. Brady, A.J. Courtenay, E. Larrañeta, M.T.C. McCrudden, D. O'Kane, S. Liggett, R.F. Donnelly, Evaluation of the clinical impact of repeat application of hydrogel-forming microneedle array patches, Drug Deliv. Transl. Res. 10 (2020) 690–705.
[85] H.R. Valera, B. Ganguly, Study of plasma level of atorvastatin and its effect on lipid profile, Indian J. Physiol. Pharmacol. 53 (2009) 73–82.
[86] P. Reddy, D. Ellington, Y. Zhu, I. Zdrojewski, S.J. Parent, J.S. Harmatz, H. Derendorf, D.J. Greenblatt, K. Browne Jr., Serum concentrations and clinical effects of atorvastatin in patients taking grapefruit juice daily, Br. J. Clin. Pharmacol. 72 (2011) 434–441.
[87] M.O. Mahmoud, H.M. Aboud, A.H. Hassan, A.A. Ali, T.P. Johnston, Transdermal delivery of atorvastatin calcium from novel nanovesicular systems using polyethylene glycol fatty acid esters: ameliorated effect without liver toxicity in poloxamer 407-induced hyperlipidemic rats, J. Control. Release 254 (2017) 10–22.
[88] K.M. El-Say, T.A. Ahmed, A.H. Aljefri, H.S. El-Sawy, R. Fassihi, M. Abou-Gharbia, Oleic acid–reinforced PEGylated polymethacrylate transdermal film with enhanced antidyslipidemic activity and bioavailability of atorvastatin: a mechanistic *ex-vivo/in-vivo* analysis, Int. J. Pharm. 608 (2021), 121057.
[89] T.A. Shaikhli, W.A. Dayyih, E. Mallah, M. Hamad, N. Qinna, T. Arafat, Determination of atorvastatin pharmacokinetic parameters by LC/MS-MS with traditional liquorice beverage, Adv. Anal. Chem. 5 (2015) 17–24.
[90] H.S. Malhotra, K.L. Goa, Atorvastatin - an updated review of its pharmacological properties and use in dyslipidaemia, Drugs 61 (2001) 1835–1881.
[91] H. Lennernas, Clinical pharmacokinetics of atorvastatin, Clin. Pharmacokinet. 42 (2003) 1141–1160.
[92] M.N. Pastore, Y.N. Kalia, M. Horstmann, M.S. Roberts, Transdermal patches: history, development and pharmacology, Br. J. Pharmacol. 172 (2015) 2179–2209.
[93] K. Srivastava, A. Arora, A. Kataria, J.C. Cappelleri, A. Sadosky, A.M. Peterson, Impact of reducing dosing frequency on adherence to oral therapies: a literature review and meta-analysis, Patient Prefer Adher. 7 (2013) 419–434.
[94] A.H. Paes, A. Bakker, C.J. Soe-Agnie, Impact of dosage frequency on patient compliance, Diabetes Care 20 (1997) 1512–1517.